

Development of a simulation model for the SuperNEMO tracker module

A thesis submitted to the University of Manchester for the degree of
Master of Science
in the Faculty of Engineering and Physical Sciences

2012

Daniel Leslie Hall

School of Physics and Astronomy

Contents

Abstract	5
Declaration	6
1 Introduction	7
1.1 Aim of this document	7
1.2 The neutrino in the Standard Model	7
1.3 The theory of double- β decay	10
1.4 Past and present experiments concerning double- β decay	12
1.5 The SuperNEMO experiment	13
2 The tracker module	17
2.1 Design of the SuperNEMO tracker	17
2.1.1 Design of an individual cell	18
2.2 The physics of a Geiger cell	19
2.2.1 The ionisation process	20
2.2.2 Drift of the electrons towards the anode	21
2.2.3 Plasma propagation and the cathode signal	26
2.2.4 The gas mixture	27
2.3 Reconstructing the particle's coordinates	28
2.3.1 Resolution of the reconstructed coordinate	32

2.4	Simulating the SuperNEMO experiment	32
2.4.1	Structure of the simulation software SNWARE	33
2.4.2	Supplementary programs	34
3	Simulating the cell response	36
3.1	Simulating the cathode response	37
3.2	Simulating the anode response	40
3.2.1	The two-dimensional fit model	41
3.2.2	The timemap model	45
3.3	Resolution of the simulated drift time	50
3.4	Implementation in the digitization process	52
4	Comparison of the models to experimental data	54
4.1	The SuperNEMO cell in Manchester	54
4.2	Applying the models	56
4.3	Re-distributing the POCI	58
5	Conclusion	63
5.1	The cathode simulation	63
5.2	Feasibility of the two models	63
5.3	Final remarks	64

List of Figures

1.1	The particles in the Standard Model.	8
1.2	The three possible distributions for the neutrino masses.	9
1.3	Diagrams for (a) double- β decay with two neutrinos and (b) neutrinoless double- β decay.	11
1.4	Diagram of the SuperNEMO demonstrator module.	13
1.5	The energy distribution expected in the presence of neutrinoless double- β decay.	15
2.1	Top down view of the SuperNEMO module used in the simulation.	18
2.2	(a) 3D view of an individual cell and (b) end-on schematic of a nine-cell array.	19
2.3	Plasma propagation along the cell.	26
2.4	An ideal event in the SuperNEMO cell.	30
2.5	The structure of the SNWARE software chain.	33
3.1	Demonstrating cell recovery. The event delay time is the time since the last event triggered in the cell. EXPAND ON THIS	39
3.2	A scatterplot of anode drift time against POCL.	42
3.3	Azimuthal dependence of parameters A and B.	44
3.4	The potential field in a standard SuperNEMO quarter cell.	45
3.5	The drift velocity to electric field relation.	46

3.6	The (a) timemap, (b) GARFIELD equivalent, (c) comparison of the two and (d) the two-dimensional fit.	49
3.7	Plot of the standard deviations of the gaussians used to fit the distribution of drift times at a given radius, using the GARFIELD Monte Carlo.	52
4.1	Simplified diagram of the 18-cell experimental setup.	55
4.2	Anode drift time distribution from the 18-celld data.	57
4.3	Comparison of the drift time models against data from the 18-cells module.	59
4.4	The distribution of POCI in the cell, as given by the SNWARE simulation discussed in setion 4.2	61
4.5	The timemap model and GARFIELD two-dimensional fit, generated using the distribution of POCI in Figure 4.4, against the data from the 18 cells. The histograms have been normalized to represent a total of 10,000 events.	62

Abstract

Abstract here

Declaration

The author hereby declares that no portion of the work referred to in the thesis has been submitted in support of an application for another degree or qualification of this or any other university or other institute of learning.

1. The author of this thesis (including any appendices and/or schedules to this thesis) owns certain copyright or related rights in it (the “Copyright”) and s/he has given The University of Manchester certain rights to use such Copyright, including for administrative purposes.
2. Copies of this thesis, either in full or in extracts and whether in hard or electronic copy, may be made **only** in accordance with the Copyright, Designs and Patents Act 1988 (as amended) and regulations issued under it or, where appropriate, in accordance with licensing agreements which the University has from time to time. This page must form part of any such copies made.
3. The ownership of certain Copyright, patents, designs, trade marks and other intellectual property (the “Intellectual Property”) and any reproductions of copyright works in the thesis, for example graphs and tables (“Reproductions”), which may be described in this thesis, may not be owned by the author and may be owned by third parties. Such Intellectual Property and Reproductions cannot and must not be made available for use without the prior written permission of the owner(s) of the relevant Intellectual Property and/or Reproductions.
4. Further information on the conditions under which disclosure, publication and commercialisation of this thesis, the Copyright and any Intellectual Property and/or Reproductions described in it may take place is available in the University IP Policy (see <http://www.campus.manchester.ac.uk/medialibrary/policies/intellectual-property.pdf>), in any relevant Thesis restriction declarations deposited in the University Library, The University Library’s regulations (see <http://www.manchester.ac.uk/library/aboutus/regulations>) and in The University’s policy on presentation of Theses.

Chapter 1

Introduction

1.1 Aim of this document

An overview of the thesis

1.2 The neutrino in the Standard Model

The neutrino is a light, neutral, weakly-interacting subatomic particle first proposed by Wolfgang Pauli in 1930 to explain how the process of single β -decay is able to conserve the overall energy, momentum and spin of the process [1]. Pauli initially named the particle the neutron, although the discovery in 1932 by James Chadwick of the more massive particle today known by that name led Enrico Fermi to rename Pauli's postulated particle the *neutrino*, meaning "little neutral one". Fermi's theory of β -decay, and by extension the neutrino, was initially met with some skepticism - however, the direct observation of the neutrino in 1956 [2] quickly cemented the particle into the pantheon of modern-day particle and nuclear physics.

Since its discovery, the neutrino has proved to be a veritable treasure trove for interesting physics. Whilst initially believed to be one particle, it is now known that three distinct

Three generations of matter (fermions)				
	I	II	III	
mass →	2.4 MeV/c ²	1.27 GeV/c ²	171.2 GeV/c ²	0
charge →	2/3	2/3	2/3	0
spin →	1/2	1/2	1/2	1
name →	u up	c charm	t top	γ photon
Quarks	4.8 MeV/c ²	104 MeV/c ²	4.2 GeV/c ²	0
	-1/3	-1/3	-1/3	0
	1/2	1/2	1/2	1
	d down	s strange	b bottom	g gluon
Leptons	<2.05 eV/c ²	<0.17 MeV/c ²	<18.2 MeV/c ²	91.2 GeV/c ²
	0	0	0	0
	1/2	1/2	1/2	1
	ν_e electron neutrino	ν_μ muon neutrino	ν_τ tau neutrino	Z⁰ Z boson
	0.511 MeV/c ²	105.7 MeV/c ²	1.777 GeV/c ²	80.4 GeV/c ²
	-1	-1	-1	±1
	1/2	1/2	1/2	1
	e electron	μ muon	τ tau	W[±] W boson
				Gauge bosons

Figure 1.1: The three generations of quarks and leptons as they lie in the Standard Model [3]. All data from [4].

flavours of neutrino exist, related to the three generations of leptons in the Standard Model: electron, muon and tau. Each neutrino carries one unit of lepton number – said unit being negative in the case of an anti-neutrino – meaning that in the β -decay process

$$n \rightarrow p + e^- + \bar{\nu}_e \quad (1.1)$$

the overall lepton number is conserved. Nowadays, the neutrinos take their place in the Standard Model as shown in Figure 1.1.

The electron neutrino has an upper mass limit of $m_{\nu_e} < 2 \text{ eV}/c^2$ [4], whilst the limits on the masses of the muon and tau neutrino are considerably higher, $m_{\nu_\mu} < 0.19 \text{ MeV}/c^2$ and $m_{\nu_\tau} < 18.2 \text{ MeV}/c^2$, respectively. Despite only the upper limit being known, the neutrinos are proven to have mass due to the phenomenon of neutrino oscillations. The effects of this were first observed in the Homestake Mine experiment in the 1960s, and later

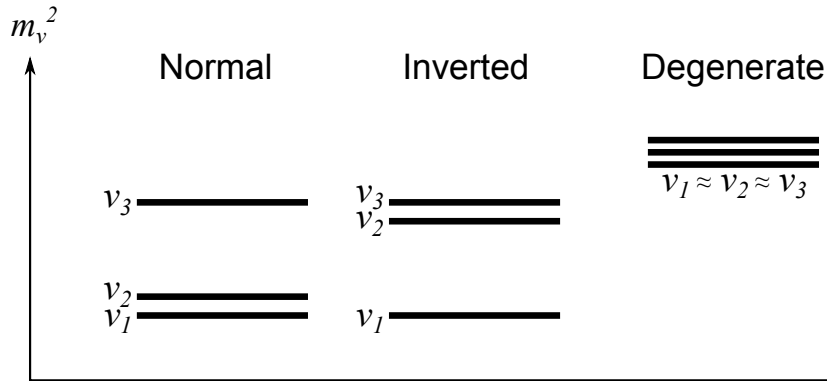


Figure 1.2: The three possible distributions for the neutrino masses.

measured directly by the Super-Kamiokande [5], SNO [6] and KamLAND [7] experiments. The oscillations arise from the fact that the weak (flavour) eigenstates of the neutrinos are not equal to their mass eigenstates, but that these are instead related via the Pontecorvo-Maki-Nakagawa-Sakata (PMNS) matrix. The two separate sets of eigenstates are related via the unitary transformation

$$|\nu_\alpha\rangle = \sum_{i=1}^3 U_{\alpha i} |\nu_i\rangle \quad , \quad (1.2)$$

where the indices α and i denote the flavour and mass eigenstates, respectively, and U is the PMNS neutrino mixing matrix.

The mass of the neutrino remains unknown, as do many details regarding its nature as a particle. The Standard Model allows for the neutrino to be a Dirac or Majorana particle (or some mixture of both, in the see-saw mechanism), although to date only its Dirac nature has been observed. A Dirac particle is defined such that its particle wavefunction $|\nu\rangle$ is not equal to its antiparticle wavefunction $|\bar{\nu}\rangle$, i.e. its charge conjugate. The reverse is true for a Majorana particle; the particle is its own antiparticle. Of further interest is the mass hierarchy of the three neutrino flavours, and whether these follow a normal, inverted or quasi-degenerate structure as illustrated in Figure 1.2. These remain open questions in particle physics, and are best investigated via the process of double- β decay.

1.3 The theory of double- β decay

Double- β decay was first proposed by Goeppert-Mayer in 1935 [8] and observed by Inghram and Reynolds in 1950 [9]. The process describes a transition from a nucleus of mass number A and atomic number Z to a nucleus of atomic number $Z + 2$,

$$(A, Z) \rightarrow (A, Z + 2) + 2e^- + 2\bar{\nu}_e , \quad (1.3)$$

via the emission of two electrons and two anti-neutrinos as seen in Figure 1.3 (a). The process has a half-life on the order of 10^{20} years [10], and as such single β -decay is always favoured when it is allowed. To study the process through experiment, β -decay must be strongly suppressed, either through conservation of energy or orbital angular momentum.

All observable double- β decays occur between even-even nuclei and require that the mass of the mother nucleus, $m(A, Z)$, be greater than the mass of the daughter nucleus, $m(A, Z + 2)$, and (for the practical purposes of forbidding standard β -decay) less than the mass of the intermediate nucleus, $m(A, Z + 1)$. The pairing effects present between nucleons in an even-even nucleus grant the latter an increased binding energy compared to even-odd and odd-odd nuclei, and this forbids standard β -decay in many even-even nuclei.

The half-life of standard double- β decay, $T_{1/2}^{2\nu}$, is given by the relation [11]

$$(T_{1/2}^{2\nu})^{-1} = G^{2\nu} |M^{2\nu}|^2 , \quad (1.4)$$

where $G^{2\nu}$ is the phase space factor and $M^{2\nu}$ is the nuclear matrix element. This form of double- β decay has been observed in 12 different nuclei [12, 13, 14].

An alternative form of the process, proposed in 1939 by Furry [15], is neutrinoless double- β decay. This is described by the transition

$$(A, Z) \rightarrow (A, Z + 2) + 2e^- \quad (1.5)$$

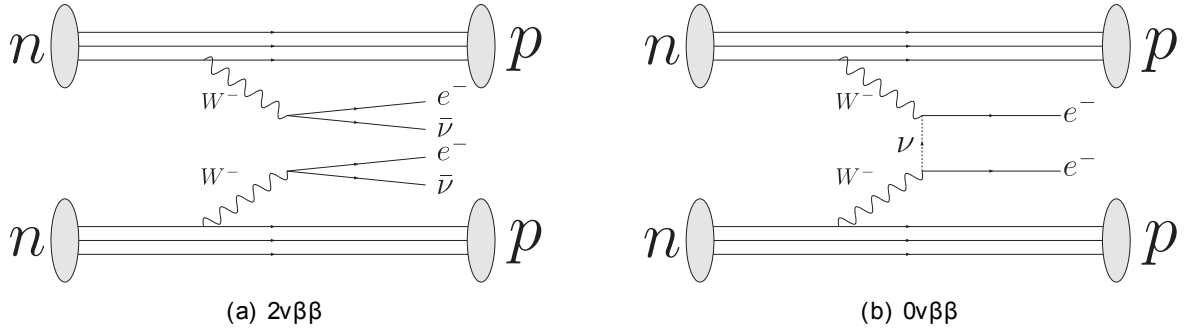


Figure 1.3: Diagrams for (a) double- β decay with two neutrinos and (b) neutrinoless double- β decay.

via the exchange of a virtual neutrino, as illustrated in Figure 1.3 b), thereby violating the conservation of lepton number. For this to occur, the neutrino must be its own antiparticle - a requirement only fulfilled if the neutrino is a Majorana particle. In contrast to the half-life described in Equation 1.4, the half-life of this process is sensitive to the effective neutrino mass $\langle m_{\beta\beta} \rangle$ [11] :

$$(T_{1/2}^{0\nu})^{-1} = G^{0\nu} |M^{0\nu}|^2 \langle m_{\beta\beta} \rangle . \quad (1.6)$$

The effective neutrino mass is related to the PMNS matrix and is defined as

$$\langle m_{\beta\beta} \rangle = \sum_{i=1}^3 m_i U_{ei}^2 , \quad (1.7)$$

where e denotes the electron components of the matrix.

The observation of neutrinoless double- β decay would mark a significant leap forward in the understanding of particle physics; a half-life for the process would place a lower limit on the neutrino mass and reveal the mass hierarchy of the three neutrino flavours. The process has not yet been observed, and it remains the focus of a number of experiments.

1.4 Past and present experiments concerning double- β decay

To date a number of experiments have been conducted with the intent of proving or not the existence of neutrinoless double- β decay, employing a number of different approaches. In general, these experiments have followed two schools of thought:

- **Source = Detector:** Experiments where the detector material is also the $\beta\beta$ source. Examples include the IGEX [16], Heidelberg-Moscow [17], Cuoricino [18], GERDA [19] and the CUORE [20] experiments.
- **Source \neq Detector:** Experiments where the $\beta\beta$ source is placed near a separate detector array. Examples are the NEMO and ELEGANTS [21] series of experiments.

The NEMO series of experiments includes the now decommissioned NEMO3 (for which NEMO and NEMO2 were prototypes) and the upcoming SuperNEMO experiment – the latter being that of interest to this study. The NEMO3 experiment [22] ran from 2003 to 2011, investigating double- β decay in seven separate isotopes : ^{100}Mo , ^{82}Se , ^{116}Cd , ^{150}Nd , ^{96}Zr , ^{48}Ca and Te, both in its natural form and as enriched ^{130}Te . So far neutrinoless double- β decay has not been observed in the collected data, and recent results have placed a lower limit on the half-life of [23, 24]

$T_{1/2}^{0\nu}$	Isotope	C.L.
$> 8.9 \times 10^{22}$ y	^{100}Mo	90%
$> 1.8 \times 10^{22}$ y	^{150}Nd	90%

Concurrent to NEMO3 was the Heidelberg-Moscow experiment, which originally placed a lower limit on the half-life $T_{1/2}^{0\nu} > 1.9 \times 10^{25}$ years [25]. A re-evaluation of the data by a sub-group of the collaboration claimed an observation of $0\nu\beta\beta$ events, with an associated half-life of $T_{1/2}^{0\nu} = (0.8 - 18.3) \times 10^{25}$ years [26]; however, this claim remains strongly

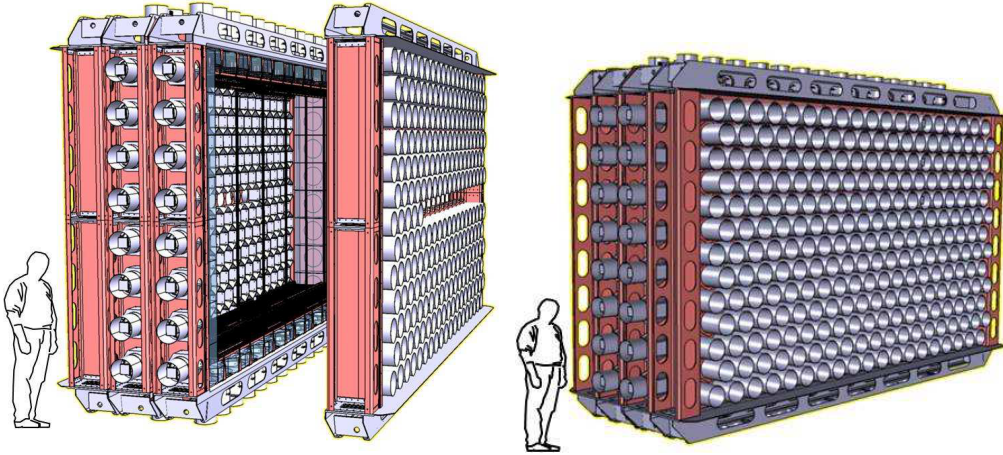


Figure 1.4: The SuperNEMO demonstrator module. The source foil (not shown) lies at the centre of a tracking volume, which is enclosed within an array of scintillators connected to photomultiplier tubes (in grey). The support structure is shown in red. Image from reference [28].

disputed [27]. Regardless of the accuracy of such a claim, it is well within the means for investigation by future experiments such as CUORE or SuperNEMO.

1.5 The SuperNEMO experiment

The SuperNEMO experiment is the successor to the now dismantled NEMO3 experiment, and like its predecessor is a source \neq detector experiment. A single source foil of either ^{82}Se or ^{150}Nd is surrounded on either side by an array of charged particle trackers and calorimeter blocks. The design of a single module is illustrated in Figure 1.4; the complete SuperNEMO experiment will consist of 20 such modules installed in the Laboratoire Souterrain de Modane. A single demonstrator module is currently under construction.

The SuperNEMO experiment is the successor to the now dismantled NEMO3 experiment, and like its predecessor is a source \neq detector experiment. A single source foil of a double- β isotope is surrounded on either side by an array of charged particle trackers and calorimeter blocks. The design of a single module is illustrated in Figure 1.4; the com-

pleted SuperNEMO experiment will consist of 20 such modules installed in the Laboratoire Souterrain de Modane. A single demonstrator module is currently under construction for both the purposes of physics and as a test-bed for the final experiment.

The particle tracking system is an array of drift tubes operating in the Geiger mode, and is described in detail in the next chapter. Mounted on either side of the particle tracker are an array of calorimeters, each unit consisting of a scintillator block attached to a photomultiplier tube. A similar array of calorimeters is mounted above and below the source foil to serve as a gamma veto. The entire module lies within a uniform magnetic field that serves to deflect the path of charged particles through the tracking volume. This is the primary advantage of SuperNEMO over other double- β experiments: with data from the tracking volume, the event reconstruction software can reliably determine the origin of a $\beta\beta$ and so remove the majority of background events not originating from the source foil. The curvature of the path of the charged particles through the magnetic field can also be used to distinguish positrons from electrons.

A double- β decay in SuperNEMO (neutrinoless or not) will be marked by the emission of two electrons that will leave a path through the tracker and be absorbed by the calorimeters. This is isolated from background events (passing electrons, other decays, spallations, etc.) by requiring the following:

1. An event consists of exactly two separate tracks and two separate calorimeter hits.
2. The curvature of the two tracks must both correspond to that expected of an electron moving through the detector.
3. Each of the two tracks must begin on the source foil and end at one of the two calorimeters that fired.
4. The two tracks must share a common vertex on the source foil.
5. The probability that the event is internal (i.e. originated from the source foil) must

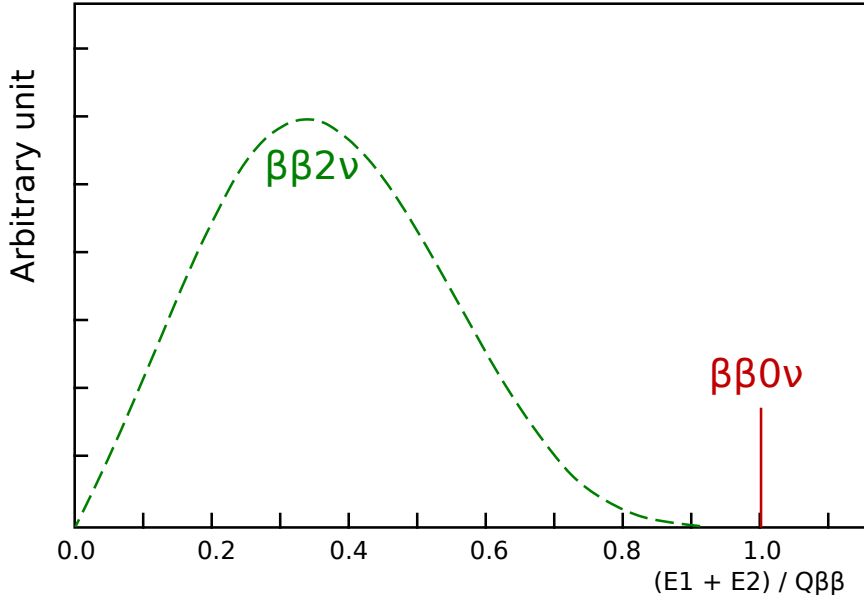


Figure 1.5: The energy distribution expected in the presence of both two-neutrino and neutrinoless double- β decay. The $\beta\beta 0\nu$ peak has been highly exaggerated for visibility.

be greater than 4% and the probability that it is external (i.e. an event crossing the detector) must be less than 1%. This is determined using the times obtained from the calorimeter hits.

6. No other tracks (prompt or delayed) must be present.
7. No photons must be present. These are indicated by a calorimeter hit with no associated track.

The major indicator of the presence of double- β decay will be a peak at the Q -value of the reconstructed electron energy. An exaggerated example of such an energy distribution is shown in Figure 1.5. The major advantage of SuperNEMO is that it is background-free; the background for the demonstrator is expected to be < 0.06 events per year. Furthermore, SuperNEMO is capable of reconstructing the angle between two electrons emitted in a double- β event. If neutrinoless double- β decay is observed, this variable will be important in understanding the underlying mechanism.

The completed SuperNEMO experiment will be sensitive to a $0\nu\beta\beta$ half-life of $T_{1/2}^{0\nu} = 1.2 \times 10^{26}$ years [28], corresponding to a neutrino mass sensitivity of ≈ 70 meV. Many details regarding the final design of the experiment, including the composition of the source foil, are still under debate.

Chapter 2

The tracker module

The SuperNEMO tracker is composed of two arrays of drift tubes – referred to as Geiger cells – operating in the Geiger mode, placed on either side of the source foil. In this chapter we will discuss the physics of such a cell and the design of an individual cell, as well as introduce the software used to simulate the SuperNEMO experiment.

A drift tube design was chosen for two of reasons: firstly, they are more cost effective per unit volume than solid-state trackers – an advantage that is further enhanced by operating them in the Geiger mode as opposed to the proportional mode. Secondly, the anode and cathode signals from a Geiger cell are on the order of 200 and 30 mV respectively and do not necessitate an amplifier directly connected to the cell. This latter advantage is especially important since it minimises the amount of electronics located near the sensitive volumes of the experiment, thus improving the design’s radiopurity.

2.1 Design of the SuperNEMO tracker

The two arrays of Geiger cells are each 9 cells deep and 114 cells wide, with the readout electronics located on top of the module and connected via a feed-through to the individual anodes and cathodes of each cell. Each array is 270 cm tall by 501.6 cm wide by 39.6 cm

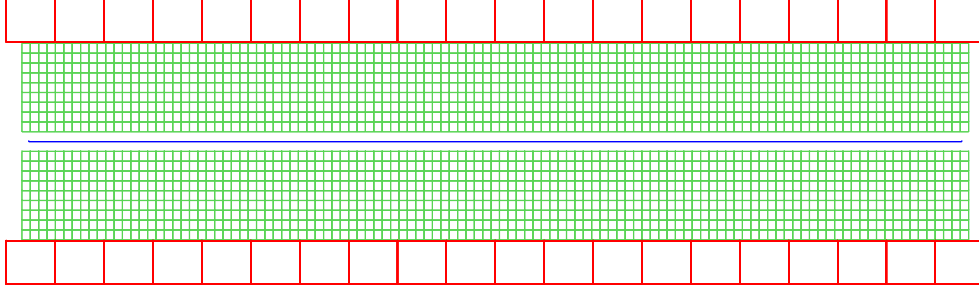


Figure 2.1: *Top down view of the SuperNEMO tracker geometry as used in the SNWARE simulation. The source foil is shown in blue and the calorimeter blocks in red. The Geiger cells are shown in green, and each cell is drawn as a square.*

deep, and begins 34 mm from the source foil. Located just beyond the tracker arrays are the two arrays of calorimeter blocks that serve to measure the energy of the traversing particles. A top-down view of the tracker as used in the simulation is shown in Figure 2.1.

2.1.1 Design of an individual cell

Each cell in the tracker array is constructed from 12 guard wires, 1 anode wire and 2 delrin end caps, one of which contains the cathode ring. Both the cathode ring and guard wires are grounded, whilst the anode wire is kept at a specified operating voltage. The guard wires are shared with the cell's neighbours and are held taut by the two end caps mounted into the tracker frame. The anode wire runs through the centre of the cell and cathode ring. The prototype cells used during this study have a cathode ring at either end for the purpose of studying the efficiency of the plasma propagation necessary to resolve the longitudinal coordinate; the cells that will be used for the demonstrator module are identical aside from only having one cathode ring, thus cutting the readout electronics by a third. The design of a prototype cell is shown in Figure 2.2.

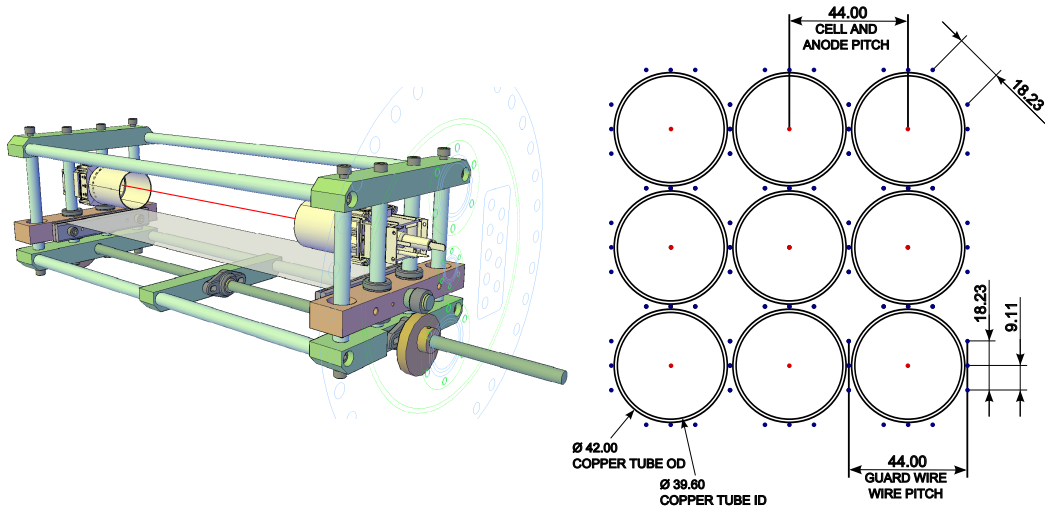


Figure 2.2: Simplified diagram of the a) side view and b) end-on view of a single SuperNEMO cell. The anode wire is shown in red and the guard wires in black. The cathode rings are shown in blue; the dashed cathode is only present in the prototype cells, and will not be used in the demonstrator module. The dashed rectangles indicate the location of the cell endcaps.

2.2 The physics of a Geiger cell

A Geiger cell is a gaseous drift tube detector operating in the Geiger mode, as opposed to the more standard proportional mode. A charged particle moving through the cell ionises the gas mixture, creating clusters of electron-ion pairs along its path. In the presence of the electric field generated by the anode wire, the electrons begin to drift towards it; conversely, the ions begin to drift towards the guard wires, although this drift is far slower by comparison. When the electrons reach the anode a signal is detected; in the proportional mode, the strength of this signal is proportional to the energy deposited by the ionising particle. This is not the case in the Geiger mode, however, and in this section we shall demonstrate how the physics of this mode allows us to reconstruct the longitudinal coordinate of the particle – at the loss of the information regarding the energy deposited. Geiger cells also suffer from a comparatively long dead time following an event – approximately 3-6 ms – although for the NEMO3 and SuperNEMO experiments, with a

trigger rate of about 0.05 Hz per cell, this does not present a problem.

2.2.1 The ionisation process

A fast electron moving through the gas in the cell creates clusters of electron-ion pairs along its path. We define the mean free path of this traversing particle between such ionising collisions to be [30]

$$\lambda = \frac{1}{N\sigma_i} , \quad (2.1)$$

where N and σ_i are the electron density and ionisation cross-section of the gas, respectively. The mean number of ionising collisions that occur over a length L is $\langle k \rangle = L/\lambda$, with a frequency described by a Poisson distribution. Thus, the probability that a number of k such ionising collisions occur along a length L is [30]

$$P(L/\lambda, k) = \frac{(L/\lambda)^k}{k!} e^{-L/\lambda} . \quad (2.2)$$

In the simplest case, we consider a homogeneous isotropic gas in which the likelihood of an ionisation occurring is independent of position. When a traversing particle loses an energy ΔE in a gas whose ionisation potential is δE , the average number of ionisation pairs created is [29]

$$\langle k \rangle = \frac{\delta E}{\Delta E} . \quad (2.3)$$

As in the case of Equation 2.2, this describes a Poisson distribution

$$P(\delta E/\Delta E, k) = \frac{(\delta E/\Delta E)^k}{k!} e^{-\delta E/\Delta E} . \quad (2.4)$$

For a path of length L through the cell during which the particle loses an energy ΔE , we sample a value from the Poisson distribution in Equation 2.4 to obtain the number of ionisations that occurred along the path. Following this, we use a uniform probability dis-

tribution to place these ionisation clusters along the path taken by the traversing particle. Once this distribution is generated, we can simulate the physics between the ionisation occurring and the signal being generated through a knowledge of the electron drift and Geiger avalanche processes.

2.2.2 Drift of the electrons towards the anode

Since the ion drift does not contribute to the cell's signal, we shall only concern ourselves with the drift of the electrons produced in the ionisation process. The study of electron drift in gaseous mixtures is a rich topic that has evolved from its simple description derived from the classical kinetic theory of gases to a much more extensive description using non-equilibrium statistical mechanics, with much of this progress having been made over the last half-century [31]. In this section we shall introduce the more transparent classical, macroscopic picture before briefly summarising the much more intricate picture painted by the solutions to the Boltzmann transport equation.

In the macroscopic theory derived from the classical model of gases, electrons in a gas possess a Maxwellian energy distribution with a mean value kT , where k is the Boltzmann constant and T the temperature of the gas. Under the influence of an electric field \mathbf{E} and a magnetic field \mathbf{B} , these electrons gain a net drift velocity \mathbf{u} . The equation of motion for these electrons thus becomes [30]

$$m \frac{d\mathbf{u}}{dt} = e\mathbf{E} + e[\mathbf{u} \times \mathbf{B}] - K\mathbf{u} , \quad (2.5)$$

where e is the charge of the electron, m its mass, and K is a friction term due to interactions with the gas. We define a characteristic time,

$$\tau = \frac{m}{K} , \quad (2.6)$$

as the mean time between collisions of electrons with molecules in the gas. We consider the case $t \gg \tau$, resulting in the steady state solution to Equation 2.5 for which $d\mathbf{u}/dt = 0$. The drift velocity vector is thus described by the linear equation

$$\frac{\mathbf{u}}{\tau} - \frac{e}{m} [\mathbf{u} \times \mathbf{B}] = \frac{e}{m} \mathbf{E} \quad (2.7)$$

To solve for the drift velocity we make the substitutions $(e/m)B_\mu = \omega_\mu$, $(e/m)E_\mu = \epsilon_\mu$, where $\mu = x, y, z$ and $\omega^2 = \sum_\mu \omega_\mu^2$, and express Equation 2.7 in the matrix form

$$M\mathbf{u} = \boldsymbol{\epsilon}, \text{ where}$$

$$M = \begin{bmatrix} 1/\tau & -\omega_z & \omega_y \\ \omega_z & 1/\tau & -\omega_x \\ -\omega_y & \omega_x & 1/\tau \end{bmatrix} \quad (2.8)$$

and for which the solution is obtained by inverting M . An alternative form for this solution is

$$\mathbf{u} = \frac{e}{m} \tau |\mathbf{E}| \frac{1}{1 + \omega^2 \tau^2} \left(\hat{\mathbf{E}} + \omega \tau \left[\hat{\mathbf{E}} \times \hat{\mathbf{B}} \right] + \omega^2 \tau^2 \left(\hat{\mathbf{E}} \cdot \hat{\mathbf{B}} \right) \hat{\mathbf{B}} \right), \quad (2.9)$$

where $\hat{\mathbf{E}}$ and $\hat{\mathbf{B}}$ are the unit vectors in the direction of the electric and magnetic fields respectively. In the absence of a magnetic field $\omega \tau = 0$, and Equation 2.9 reduces to [30, 31]

$$\mathbf{u} = \frac{e}{m} \tau \mathbf{E} = \mu \mathbf{E}, \quad (2.10)$$

where $\mu = e\tau/m$ denotes the scalar mobility. For non-zero magnetic fields, the mobility μ becomes a tensor given by $(e/m)M^{-1}$. In the SuperNEMO experiment a magnetic field is present and, when considering a cross-section of the cell perpendicular to the anode wire, orthogonal to the electric field at most points in the cell, i.e. $\mathbf{E} \cdot \mathbf{B} = 0$. Although this does not apply in the proximity of the cathodes, this feature is important when considering

the effect of the magnetic field upon the drift of the electrons towards the anode.

We define the $x - y$ plane to be perpendicular to the anode wire and centred upon a drifting electron, with the positive x -axis defined as being in the direction of the electric field currently experienced by the electron. In this frame of reference, $\mathbf{E} = (E_x, 0, 0)$ and $\mathbf{B} = (0, 0, B_z)$; Equation 2.9 thus reduces to three components for \mathbf{u} :

$$\begin{aligned} u_x &= \frac{(e/m)\tau}{1 + \omega^2\tau^2} |\mathbf{E}| \\ u_y &= \frac{(e/m)\tau}{1 + \omega^2\tau^2} \omega\tau |\mathbf{E}| \\ u_z &= 0 \end{aligned} \tag{2.11}$$

The tangent of the angle ψ between the x and y components of \mathbf{u} is defined as

$$\tan \psi \equiv \frac{u_y}{u_x} = -\omega\tau \tag{2.12}$$

and thus the magnitude of \mathbf{u} is given by

$$|\mathbf{u}| = \frac{(e/m)\tau}{\sqrt{1 + \omega^2\tau^2}} |\mathbf{E}| = \frac{e}{m}\tau |\mathbf{E}| \cos \psi \tag{2.13}$$

and its direction by

$$\hat{\mathbf{u}} = \frac{\hat{\mathbf{E}} + \omega\tau \left[\hat{\mathbf{E}} \times \hat{\mathbf{B}} \right]}{\left| \hat{\mathbf{E}} + \omega\tau \left[\hat{\mathbf{E}} \times \hat{\mathbf{B}} \right] \right|} . \tag{2.14}$$

The product $|\mathbf{E}| \cos \psi$ is the component of the electric field in the direction of the drift velocity; this relation implies that the functional dependence of $|\mathbf{u}|$ on $|\mathbf{E}|$ and $|\mathbf{B}|$ is

$$|\mathbf{u}| = F(E, B) = F(E \cos \psi, 0) , \tag{2.15}$$

a result known as Tonk's theorem [30, 32]. The result of this functional dependence is that whatever the direction of the electron drift, the magnitude of $|\mathbf{u}|$ is determined by the component of the electric field in the drift direction for any magnetic field, provided that $\mathbf{E} \cdot \mathbf{B} = 0$ and that τ is constant [30]. This result has been verified experimentally for fields up to 12 kG [30].

Another aspect of the electron drift is diffusion; as the electron cluster travels towards the anode it will spread according to a diffusion coefficient D . The mechanics of this diffusion process is described in reference [30]. In the classical limit the distribution of an electron cluster along a direction x , beginning point-like at a time $t = 0$, is described by a Gaussian distribution with a standard deviation

$$\sigma_x^2 = 2Dt , \tag{2.16}$$

where D is a field-dependent diffusion coefficient. Until 1967 it was always assumed that the diffusion of the cluster was isotropic, until work by Wagner et al [33] demonstrated otherwise: the diffusion coefficient along the electric field varies substantially from that perpendicular to it. As the electric field increases – and with it, the average energy of the electrons – the ratio $D_L/D_T < 1$, where D_L and D_T are the coefficients for diffusion parallel and perpendicular to the electric field [30]. This means that the electron cluster is described by two separate Gaussian distributions, the wider of the two describing the spread transverse to the drift direction – an effect known as electron anisotropy. The description just given relies on there being no magnetic field present; if this is not the case, the more complicated effect of magnetic anisotropy manifests itself, at which point the diffusion coefficient is represented by a 3×3 tensor.

It is here that the classical theory outlives its usefulness and we must turn to the complete microscopic theory for a more accurate picture directly related to the cross-sections of the molecules in the gas mixture. The classical theory relies upon the electron

energy distribution remaining Maxwellian under the influence of an electric field. While this may hold for some gases such as carbon dioxide (a so-called “cool” gas), electric fields of only a few V / cm in Argon are enough to considerably increase the average electron energy [31]. The microscopic theory usually relies either upon finding solutions to the Boltzmann transport equation [34] or Monte Carlo simulations of the movement of individual electrons in the gas mixture at the microscopic level [35]. Some drift simulation programs such as MAGBOLTZ use a mixture of both methods. The classical theory is also not able to account for electron or magnetic anisotropy. Hence, in this study we shall rely upon the classical theory when it is appropriate to do so, apart from the calculation of drift velocities and diffusion coefficients where the microscopic theory as used by MAGBOLTZ, whose function and output is further discussed in section 2.4.2.

In a SuperNEMO cell, the geometry is such that an electron anywhere in the cell should ultimately be drawn to the anode wire by the electric field, with the drift velocity being greater the closer the electron is to the wire. Hence, when the electron-ion clusters are formed along the path of the particle through the cell, it is the cluster closest to the wire that will be responsible for the start of the anode signal. The signal detected is a charge collection signal, and is proportional to the rate of electron capture; once the cell has been completely ionised and all electrons have been captured upon the wire, the signal stops. The location of the nearest electron cluster to the wire is known as the point of closest ionisation – hereafter referred to as the POCI – and is ultimately what is resolved from the coordinate reconstruction. The fact that the POCI does not necessarily correspond to the point of closest approach between the traversing particle and the anode wire accounts in part for the resolution of the cell.

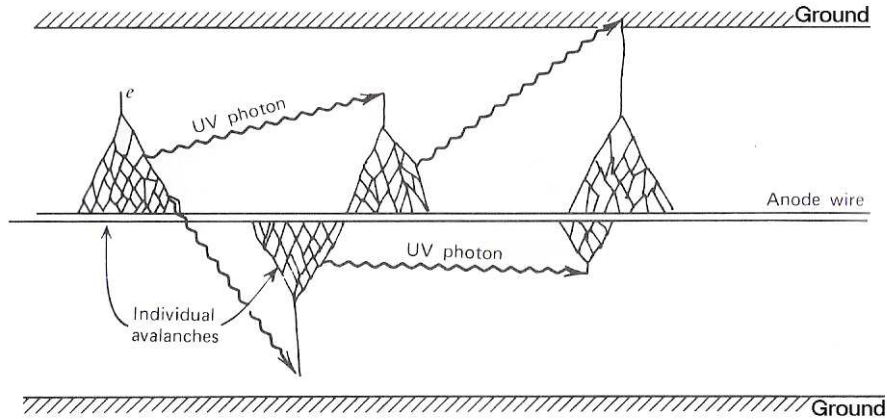


Figure 2.3: Plasma propagation along the cell in the Geiger mode. The avalanche process that occurs in the proximity of the wire (here shown in exaggerated scale) emits UV photons that travel to nearby regions of the cell. These trigger further ionisations in the un-fired regions of the cell either side of the original avalanche.

2.2.3 Plasma propagation and the cathode signal

As the electrons approach the wire they ionise the gas in their path, producing more electron-ion pairs in proportion to the strength of the local electric field. In a cell design such as that used in SuperNEMO the electric field increases strongly in the region close to the wire, which results in the drifting electrons generating a Townsend avalanche in the proximity of the wire. This is illustrated in Figure 2.3.

The energy of the electrons in the Townsend avalanche is such that bremsstrahlung results in the emission of UV photons. These photons travel a short distance before ionising the gas elsewhere in the cell. Since the region of the cell where the original ionisation occurred has since been depleted, this ionisation occurs a short distance either side of this region. This leads to a knock-on effect whereupon this UV ionisation generates further Townsend avalanches and in turn more UV photons, each time affecting the non-ionised region adjacent to the avalanche. The result is a positively charged plasma that propagates lengthways down the cell in both directions until the entire cell has been ionised.

Studies in NEMO3 [22] have shown that the speed with which the plasma propagates

longitudinally down the cell is approximately constant, until it reaches the ends of the cell and enters the cathode ring. When the plasma enters the cathode ring, the sudden depletion of electrons generates a positive electric field, which in turn induces a negative charge on the inside of the cathode ring. To neutralise this field electrons are drawn from the ground, generating a potential drop between the ground and the cathode; this potential is detected by the electronics as a signal to which a timestamp is applied. In section 2.3 we will demonstrate how the anode and cathode signal can be used to reconstruct the longitudinal coordinate of the traversing particle.

2.2.4 The gas mixture

The gas mixture in a NEMO3 cell is He-4 (95%), Ar-18 (1%) and Ethyl alcohol (4%) – percentages are quoted by volume. Helium was chosen as the major gas in the mixture due to being unreactive and of low atomic number, thus reducing the amount of energy deposited by the traversing particle. Argon was added to the mixture after studies [22] demonstrated that it improved the stability of the longitudinal plasma propagation, as well as reducing problems associated with cell ageing.

The SuperNEMO gas mixture is currently on track to being identical to that used in NEMO3, although contemporary studies in which the argon is replaced with neon have shown promising preliminary results. During this study the two gas mixtures that were used for experiment were the standard NEMO3 mixture and helium/neon/alcohol in the volume ratio of 94/2/4 percent.

The Ethyl alcohol serves as a quenching gas, whose purpose is to prevent double-firing of the cell due to the He/Ar/Ne ions creating secondary electron-ion pairs upon reaching the guard wires. When these ions are neutralised by the guard wires, there is a small likelihood that the process will generate further electrons. These will then drift towards the anode and generate a false signal. The quenching gas has a lower ionisation energy than

Helium, Argon and Neon, and when these drifting ions collide with the Ethyl molecules the latter neutralise the former. The resulting Ethyl ions then drift towards the guard wire, with the final outcome being that the ions arriving at the guard wire are those of the quenching gas. The more complicated molecular structure of the Ethyl alcohol inhibits the creation of secondary electron-ion pairs and greatly decreases the probability of a false signal.

2.3 Reconstructing the particle's coordinates

The ideal output of a SuperNEMO prototype cell is shown in Figure 2.4 – the two major differences between this and the true SuperNEMO cell is that in Figure 2.4 two cathodes signals are present as opposed to one, and no calorimeter signal is present. The data extracted from this event are four times: the time the anode signal begins t_{anode} , the time the first (negative) peak on the anode derivative signal begins t_{deriv} , and the time of the first and second cathode peaks t_{c1} and t_{c2} . These last two can also be extracted from the anode derivative signal by searching for two neighbouring peaks, the first being negative and the second being positive. An example of this two-peak feature in the derivative signal can be seen at B and C in Figure 2.4. However, to resolve the left/right ambiguity during coordinate reconstruction, at least one cathode signal must be present.

All the important features of a cell event are present in Figure 2.4. The anode signal begins and increases to a maximum as the rate of electron collection becomes constant; this signal then halves when the plasma reaches one of the cathodes. The sudden spike in the anode signal immediately before the drop is due to the difference in the electric field experienced by the electrons within the cathode ring. The cathode rings are grounded but of a lesser radius than the side length of the cell, hence the electric field within the cathode ring is greater. When the gas within the ring is ionised, the electrons drift towards the anode faster than those generated in the main body of the cell, resulting in a short spike

in the signal. This effect is seen at features B and C in Figure 2.4 and is responsible for the two-peak features on the derivative signal. Once the plasma has reached both ends of the cell the gas has been completely ionised, and the anode signal drops to below the original voltage as the remaining positive ions counteract the potential field generated by the anode wire. The anode signal steadily increases back to the original value as the ions neutralise on the guard wires. It should be noted that the anode signal does not actually lie at 0 mV – a constant value, referred to as the *pedestal*, is subtracted from the data by taking the integral of the anode voltage in the early region of the event window with no signal, and dividing said integral by the difference between its limits. If the cell had not completely recovered or if a signal was present in the beginning of the window – where no signal should be present, since the triggered signal should begin at a preset time in the window – then the pedestal value will differ from that of an ideal event. This allows a cut to be made during analysis to isolate only those events with a pedestal value close to the ideal, removing a number of bad events in which the cell may still be recovering.

A further important time is that of the associated calorimeter array, t_{calo} . In the timescale of the electron drift from the POCI to the wire, the electron time-of-flight from the cell to the calorimeter is negligible – hence, t_{calo} is taken to be the time that the POCI is generated. From this, we take the drift time from the POCI to the anode wire to be $t_{drift} = t_{anode} - t_{calo}$; the anode derivative time is used as a sanity check, since ideally $t_{anode} \approx t_{deriv}$.

From this data, it is possible to reconstruct the longitudinal and radial coordinate of the point of closest ionisation (POCI) of the electron to the cell anode wire. We consider the cylindrical coordinate system $\mathbf{r} = (r, \theta, z)$, where the z -axis is along the anode wire (with $z = 0$ halfway down the cell) and the (r, θ) plane is perpendicular to and centred at the anode wire. The coordinate $\mathbf{r} = (0, \theta, 0)$ corresponds to a point lying at the centre of the anode wire halfway along the cell. We define cathode 1 as lying in the region $z < 0$ and cathode 2 at $z > 0$.

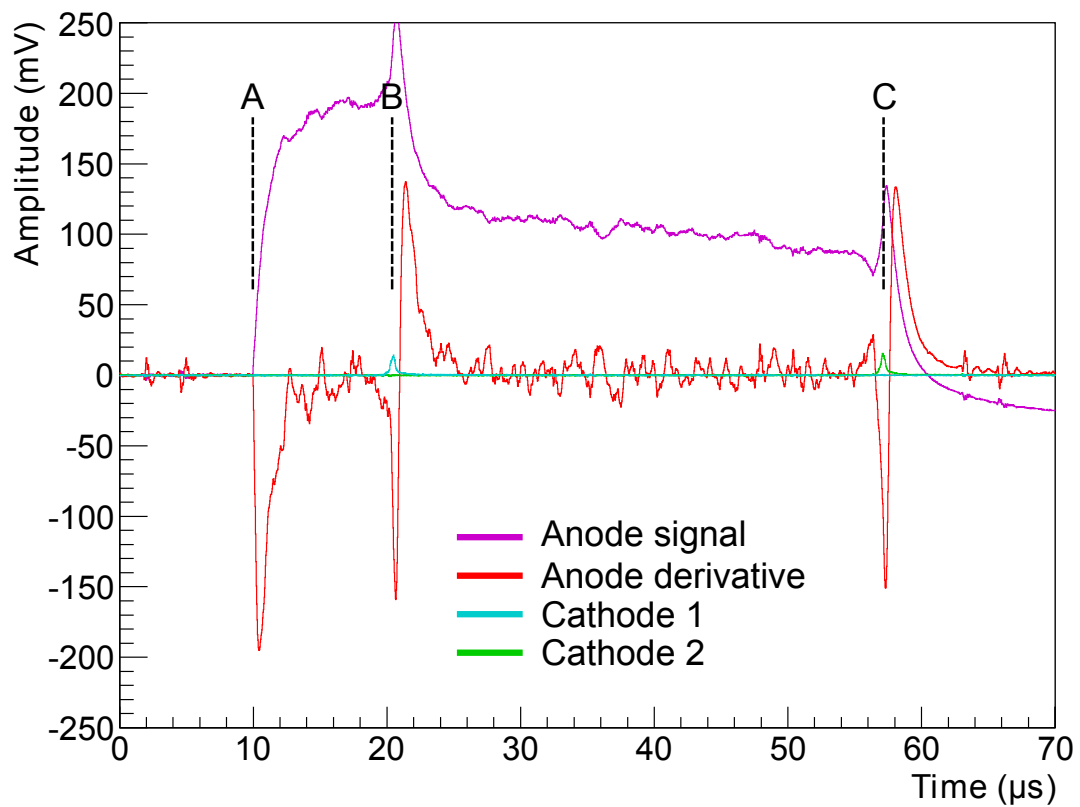


Figure 2.4: A typical event in the prototype cell, with both cathodes operating. The anode charge collection begins at feature A, and the plasma reaches cathodes 1 and 2 at features B and C respectively.

The z -coordinate is determined from the cathode times t_{c1} and t_{c2} , via the relation [22]

$$z = \frac{L_{eff}}{2} \frac{t_{c2} - t_{c1}}{t_{c2} + t_{c1}} \left[1 - K \frac{L_{eff}}{2} \left(1 - \left| \frac{t_{c2} - t_{c1}}{t_{c2} + t_{c1}} \right| \right) \right] \quad (2.17)$$

where L_{eff} is the effective length of the cell, the distance along the z -axis from the edge of cathode 1 to the edge of cathode 2, and $K = 0.408 \times 10^{-4}$ is a constant. The first order component is that which assumes a constant plasma propagation speed along the cell. The second component accounts for the reduced plasma propagation speed that is due to a decrease in the high voltage during propagation. This last term is dependent upon the voltage on the anode and the gas mixture, and the value of K quoted is that used in NEMO3.

The anode reconstruction can be done through two sets of relations. For NEMO3, first analyses were done using the following equations [36]:

$$r = \begin{cases} 0.025 & t_{drift} = 0 \\ (0.598 + 0.0045t_{drift}) & 0 < t_{drift} < 60 \\ (-0.292 + 0.023t_{drift}) & 60 < t_{drift} < 220 \\ (0.22t_A^{0.572}) & 220 < t_{drift} < 1480 \\ 14.3 & t_{drift} \geq 1480 \end{cases} \quad (2.18)$$

with the radius r given in mm and t_{drift} in nanoseconds. Subsequent analyses have used a single relation

$$r = \frac{6.759t_{drift}}{t_A^{0.84} + 287.09} + 0.1877 \quad (2.19)$$

although this relation does not so well apply for anode times of $t_{drift} < 60ns$, for which the old relation is used.

2.3.1 Resolution of the reconstructed coordinate

In NEMO3, the resolution on the radial (i.e. transverse) and longitudinal coordinate are considered separately. The transverse resolution is given by the relation [22]

$$\sigma_{\perp} = \sqrt{\sigma_{int}^2 + k \left(\frac{\sqrt{L_{track}}}{E} \right)^2} \quad (2.20)$$

where $\sigma_{int} = (0.37 \pm 0.02)$ mm is the intrinsic radial resolution, L_{track} is the length of the particle's path through the cell, E is the initial energy in keV of the particle when it entered the cell, and $k = (10.8 \pm 1.7)$ mm keV² is a fitting constant. The values quoted are those used in the NEMO3 analyses.

The longitudinal resolution follows a similar relation that is dependent upon the longitudinal coordinate, with [22]

$$\sigma_{\parallel} = \sigma_0 \sqrt{1 - \left(\frac{2z}{L_{eff}} \right)^2} \quad (2.21)$$

where L_{eff} is the effective length of the cell and $\sigma_0 \approx 1.1$ cm is the maximum resolution on the longitudinal coordinate possible for a POCI at the mid-length of the cell.

2.4 Simulating the SuperNEMO experiment

In this section we will briefly summarise the software utilised throughout this study. Of greatest importance to simulating the SuperNEMO experiment is the SNWARE software chain, which consists (at time of writing) of the software packages Cadfael, Channel, Bayeux and Falaise. In addition to these, the electron drift simulations MAGBOLTZ and GARFIELD were used alongside the specially developed software packages Timemap and CellSolver.

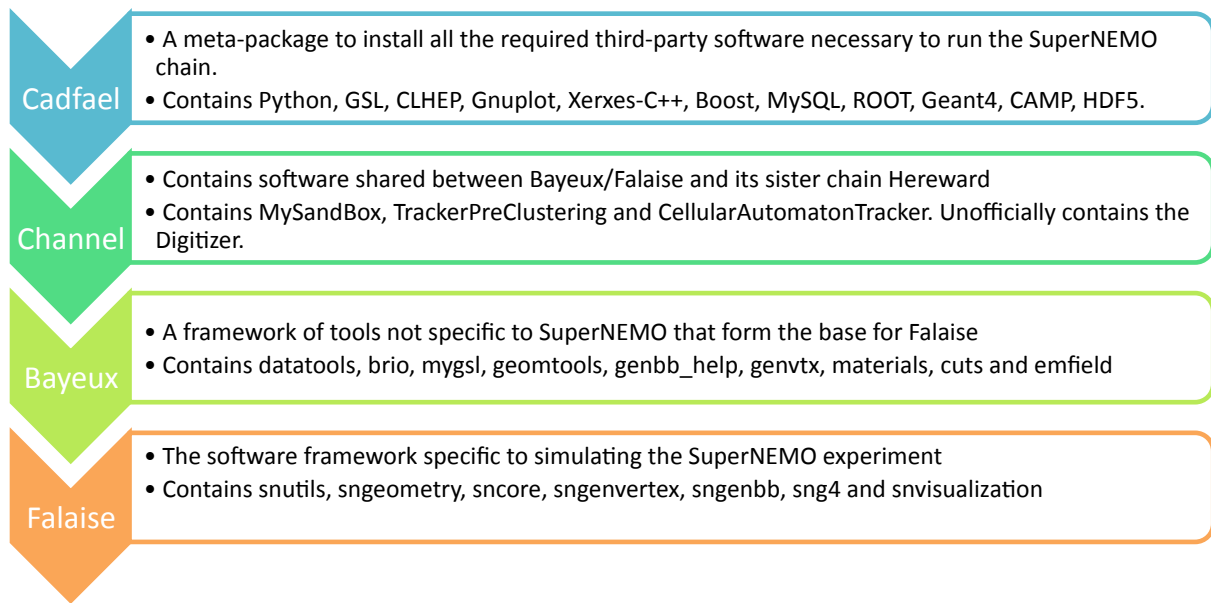


Figure 2.5: The structure of the SNWARE software chain, correct as of 29/06/2012. Each package is dependent upon the one above it.

2.4.1 Structure of the simulation software SNWARE

The SNWARE [37] software chain is a series of software packages intended to simulate the entirety of the SuperNEMO experiment and to analyse the output, both from the simulation and from the real data collected by the future experiment. The software chain is comprised of 4 separate parts – Cadfael, Channel, Bayeux and Falaise – whose components and major function are summarised in Figure 2.5.

Cadfael serves as an aggregator package, installing on the user’s system the collaboration-approved versions of the necessary third-party software. The Channel package contains software common to both the Bayeux/Falaise packages and to SNWARE’s sister software chain Hereward, which is used in NEMO3 analyses. Bayeux is a series of general-purpose software packages developed for use at LPC Caen, capable of dealing with data input/output (datatools/brio), geometry management (geomtools/materials) and vertex generation (genvtx/genbb_help). This forms the framework for Falaise, whose packages are specially designed to simulate the SuperNEMO experiment – although they can be

adapted to arbitrary geometries. The particle simulation itself is done using GEANT4 via the sng4 module. Additionally, when the simulation is run, the user has the option of loading custom-built modules into the simulation for various purposes; an example is the ROOTIO module, that saves each event as it occurs into a ROOT file suitable for easy analysis at a later date. At time of writing, the software chain is still in beta and undergoing constant development, so the reader is cautioned that this information may not be up-to-date.

2.4.2 Supplementary programs

In addition to the SNWARE software chain, four further software packages are used throughout this study; these are MAGBOLTZ [38], GARFIELD [39], CellSolver [40] and Timemap. MAGBOLTZ simulates the drift of electrons in arbitrary gas mixtures under the influence of electric and/or magnetic fields by solving the Boltzmann equation; the output is used in the both the GARFIELD and Timemap packages. The output includes the drift velocity (separate values for x , y and z), the diffusion coefficient (both parallel and transverse to the electric field) and the electron energy distribution for a specified electric field. To obtain the drift velocity to electric field relation required by both GARFIELD and Timemap, MAGBOLTZ must be run for a range of electric fields.

GARFIELD simulates particle drift chambers in 2 or 3 dimensions, using interfaces to both MAGBOLTZ and HEED [41]. The latter serves to simulate the initial ionisation in the chamber due to a traversing particle, and is not used in this study in lieu of the mechanism described in section 2.2.1. GARFIELD can solve for arbitrary electric and magnetic fields in two dimensions, but not to great accuracy; instead, the software relies on importing field solutions from commercial software such as ANSYS Maxwell.

CellSolver [40] and Timemap are packages specially developed for this study. CellSolver solves for the electric field in a SuperNEMO quarter cell using a successive over-relaxation

(SOR) method, with the user specifying the voltage on the anode wire and the number and location of the guard wires. The CellSolver code has been incorporated into the Timemap package, which is a C++ class designed to simulate the electron drift towards the anode in a SuperNEMO cell, using the timemap model described later in section 3.2.2.

Chapter 3

Simulating the cell response

To achieve an effective simulation of the experiment, it is important that the response of each individual Geiger cell is modelled correctly to obtain a realistic set of anode and cathode times. The response of each cell is divided into three stages: the ionisation process, the drift of the electrons towards the anode, and the propagation of the plasma towards the cathodes, occurring in that order. In this chapter we shall first discuss the cathode simulation as it was done in NEMO3 and conclude as to whether any modifications are necessary. We shall then introduce a number of models that can be used to simulate the drift of the electrons from the POCI to the anode wire, and discuss their effectiveness. Finally, we will briefly explain how the simulation of an individual cell is incorporated into the overarching simulation of the entire experiment.

Once the SNWARE simulation is complete, what remains is a data file containing information about each event that occurred, stored in sequential order. The information stored is that of the “true” physics; the momentum of each particle after every step, the location of every interaction, and so on. The next step is to translate this data model into one identical to that of the output from the actual SuperNEMO experiment. During this conversion, the response of the detector must be modelled to accurately reflect the behaviour of the Geiger cells and their electronics. In this chapter we will discuss a number

of models that can be used to simulate the response of a Geiger cell in the tracker module; these will be tested against data in the succeeding chapter. It should be noted that these are not digitization models in the strictest sense of the word – the true process of digitization is to convert simulation data into data words of the kind outputted by the SuperNEMO electronics. However, such a process must necessarily encompass the simulation of the tracker and for the purposes of nomenclature these digitization models will be referred to as such henceforth. The response of the calorimeter (and its respective digitization model) is a study in and of itself, and will not be considered here.

3.1 Simulating the cathode response

As discussed previously, the cathodes require the plasma to propagate from the interaction point to the inside of the cathode ring for a signal to be generated. Data [42] taken with an 18-cell module using cosmic ray muons shows that the plasma propagation efficiency is better than 99%, provided that there is no dust on the anode wire. The presence of dust at a location on the wire inhibits plasma propagation beyond this point and can reduce this efficiency to as low as 30%.

Studies in NEMO3 have shown that the plasma propagation speed is approximately constant, as implied in the (quasi-)linear relation seen in Equation 2.17. In the NEMO3 simulation, the cathode time simulation is done assuming a linear relationship between longitudinal position and time (i.e. Equation 2.17 with $K = 0$) and a constant plasma velocity. Given the longitudinal coordinate of a POCl, the cathode times are given by

$$\begin{aligned} t_{c1}^{(N3)} &= \frac{L_{eff} + 2z}{2v} \quad \text{and} \\ t_{c2}^{(N3)} &= \frac{L_{eff} + 2z}{2v} , \end{aligned} \tag{3.1}$$

where z is the longitudinal coordinate, L_{eff} the effective length of the cell and v the velocity of the plasma. The cathode times $t_{c1}^{(N3)}$ and $t_{c2}^{(N3)}$ are explicitly those times given by the

Event type	Description
Full	Both cathodes in the event have a signal with amplitude over 5 mV
Partial	Only one cathode in the event has a signal above 5 mV
No cathode	Neither cathode has a signal above 5 mV

Table 3.1: Definition of event types in the Geiger cell.

NEMO3 simulation, and represent the time it takes for the plasma to propagate from a point z along the wire to their respective cathode. Since the plasma does not start to propagate until the first avalanche begins this means that

$$\begin{aligned}
 t_{c1} &= t_{drift} + t_{c1}^{(N3)} \quad \text{and} \\
 t_{c2} &= t_{drift} + t_{c2}^{(N3)} .
 \end{aligned}
 \tag{3.2}$$

However, the NEMO3 simulation does not simulate the electron drift, so there is no value of t_{drift} present to offset the cathode times to their realistic values.

A constant plasma velocity implies a constant plasma propagation time, i.e. that $t_{c1} + t_{c2} \approx \text{constant}$ for all events. However, data taken with a single SuperNEMO cell triggering on cosmic ray muons [42] shows that the plasma propagation time is actually a function of both the time since the last event in the cell – the *event delay* – and the nature of this previous event. We define the nature of the event in one of three ways according to its cathode signal, as given in table 3.1. As seen in Figure 3.1 (a), the plasma propagation time increases exponentially for event delays of less than 5 ms, and far more non-full events are seen at short event delays. This implies that the plasma propagation is hindered by the recovery of the cell; as fewer non-ionised particles are present in the cell, the probability that a UV photon generated during a Townsend avalanche causes further ionisation down the cell is decreased. This results in a slower propagation velocity with a greater chance that the propagation will halt before reaching the cathode. The lower number of non-ionised particles also results in a reduced amplitude on the anode signal, as seen in Figure 3.1 (b).

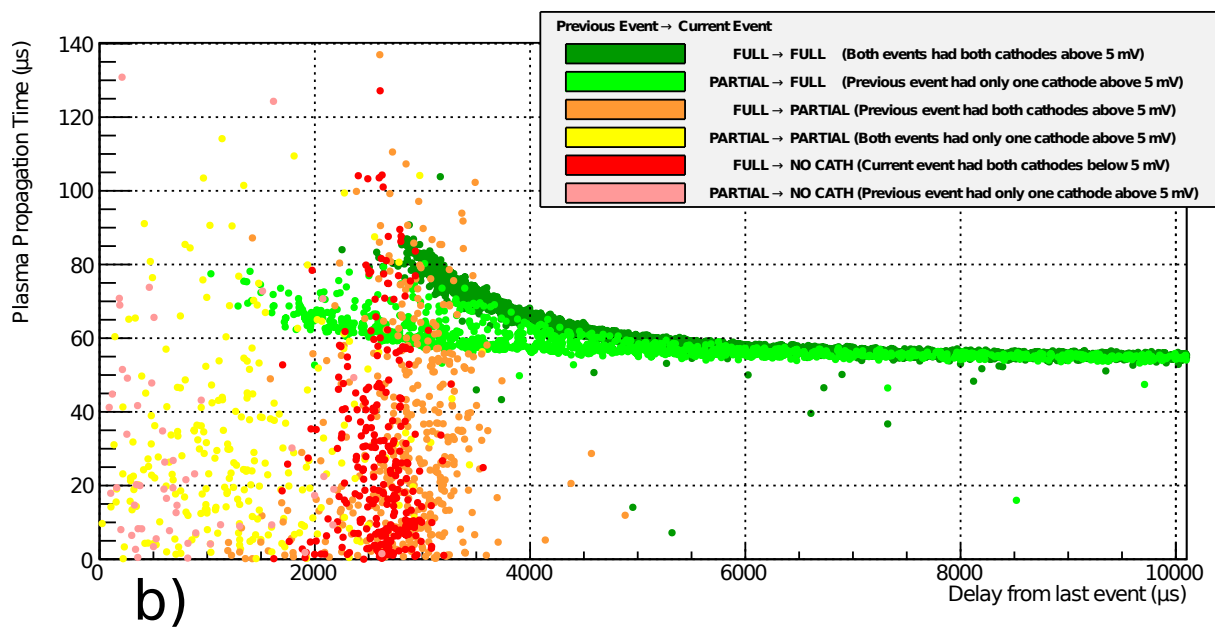
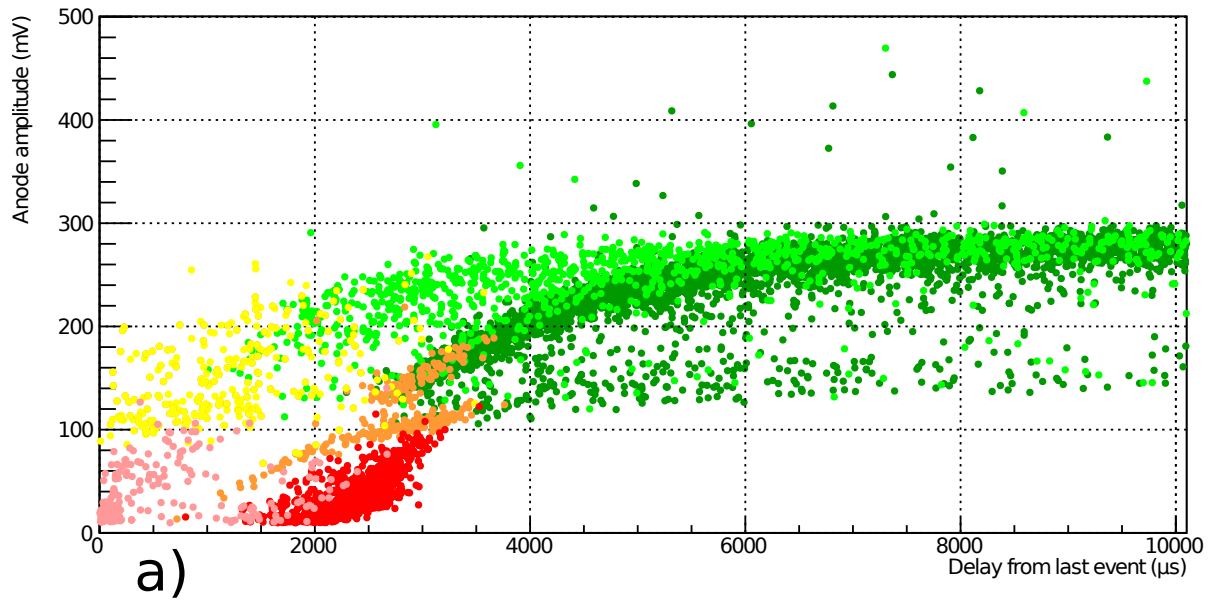


Figure 3.1: Demonstrating cell recovery. The event delay time is the time since the last event triggered in the cell. *EXPAND ON THIS*

It also appears that the cell is capable of recovering comparatively faster from partial events. This can be seen in Figure 3.1 (a) where full events succeeding a partial one demonstrate shorter plasma times than those succeeding a full one of a similar event delay. However, since during these events the cell is recovering in a non-homogeneous manner, there is little guarantee that the plasma propagation is constant along the length of the cell.

However, event rates in SuperNEMO are expected to be ≈ 0.3 Hz per cell, and so it is highly unlikely that the effects of cell recovery will be observed in the data. Furthermore, the reconstruction of the longitudinal coordinate relies on the ratio of the two cathodes times and not on the absolute value of the propagation time, nor on the offset presented by t_{drift} in Equation 3.2. Therefore we can conclude that it is not necessary to amend the cathode simulation model used in NEMO3 for use in SuperNEMO, although the inclusion of the drift time offset is recommended.

3.2 Simulating the anode response

As mentioned in section 3.1, the NEMO3 simulation does not simulate the drift of the electrons from the POCI and the resulting anode signal; instead the distance of the POCI from the anode wire is given directly, bypassing the need to reconstruct the radial coordinate in the manner described in section 2.3. In SuperNEMO it is necessary to simulate the electron drift and extract a realistic drift time for two reasons: firstly so that the simulation output better matches that of the actual experiment, and secondly so that the effectiveness of the reconstruction methods can be tested against the simulation. In this section we will describe to separate methods that can be used to simulate the electron drift in the Geiger cell.

In simulating the anode response we concern ourself primarily with two factors: the shape of the electric potential within the cell and the dynamics of electron drift towards

the anode. To do so, two separate approaches are used; the first, referred to as the two-dimensional fit model, involves simulating the cell in GARFIELD and modelling the electron drift, developing a one-to-one functional form between the POCI and the drift time. The second approach is to develop a C++ module for the simulation software capable of solving for the electric potential in the cell and simulating the electron drift directly. The latter is referred to as the timemap model, and is benchmarked against results given by the tried-and-tested GARFIELD [39] program.

3.2.1 The two-dimensional fit model

In the two-dimensional fit model we seek to find a functional form that describes the relationship between the coordinate of the POCI in the plane of the cell and the resulting anode drift time given by the electronics. This fit is made using a simulation of the Geiger cell done using GARFIELD, which is commonly used in these situations.

We consider a cross-section of a single SuperNEMO cell, with the x - y plane perpendicular to the anode and guard wires. GARFIELD is capable of solving Poisson's equation for the cell and, via an interface with the MAGBOLTZ program, simulating the drift of an electron from a point (x, y) to its collection on the anode wire. GARFIELD has three such function calls for this purpose: Microscopic, Runge-Kutta and Monte Carlo. The Microscopic function utilises the Monte Carlo microscopic theory mentioned in section 2.2.2, and whilst being the most accurate of the three is only computationally efficient for a few drift calculations over a short distance. The Runge-Kutta method solves for the equations of motion given by the macroscopic theory, whilst the Monte Carlo method simulates the motion of an electron at the microscopic level, accounting for diffusion. We used the latter method to construct a distribution of the anode drift time t_{drift} as a function of the radius to the POCI (x, y) , as shown in Figure 3.2.

It is evident that the presence of the guard wires and the cuboid geometry of the cell

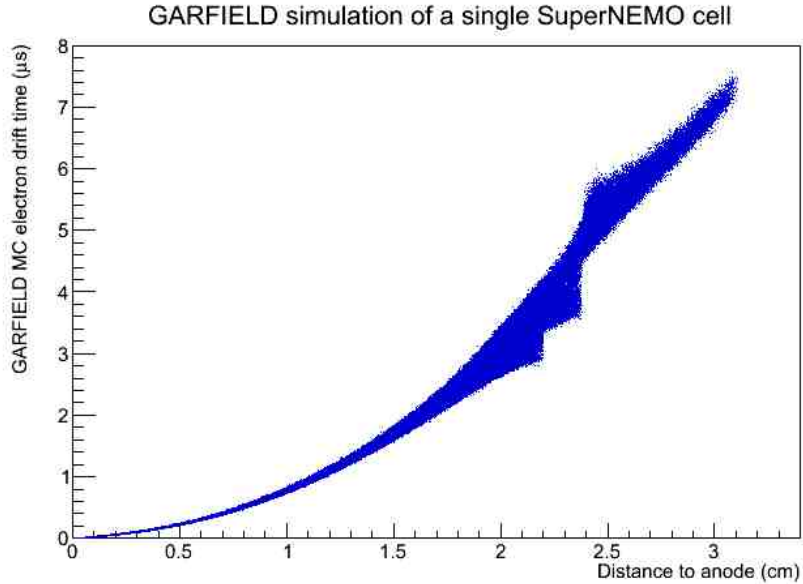


Figure 3.2: A scatterplot of anode drift time against POCI. Generated using GARFIELD’s `MC_electron_drift` function call.

imposes a significant azimuthal dependence upon the relationship between drift time and radius of the primary ionisation, particularly for radii greater than 1.5 cm from the wire. In a first attempt at a drift-time model, we naively ignore the azimuthal dependence, and propose a relation of the form

$$t_{drift} = Ar^B \quad (3.3)$$

where r is given in mm and t_{drift} in μs . We now consider a segment of the cell described by a sweep centred at the origin of a small angle $d\theta$, with $\mathbf{r} = (r, \theta = 0)$ being defined as a vector pointing along the positive y -axis. The drift time distribution of the POCI that lie in this small area dA is much better described by the one-to-one fit given in Equation 3.3. To extend the model into two dimensions, we apply the fit to each area dA given by $\theta + d\theta$, proceeding clockwise round the cell. This process is repeated twice, first fitting only to radii less than 1.5 cm and secondly for radii in the range $1.5 < r < 2.0$ cm. The

result is two pairs of parameters, (A_{close}, A_{far}) and (B_{close}, B_{far}) , whose θ dependence is shown in Figure 3.3.

In the close region, both parameters A and B have been fitted with a function of the form

$$A_{close}, B_{close} = \alpha_{A,B} \cos(\beta_{A,B}\theta) + \gamma_{A,B} \quad (3.4)$$

where α, β, γ are the six separate fit parameters, although the approximation can be made that the period $\beta_A = \beta_B$, reducing the number of required parameters to five. In the far region, a more complicated relation is required, of the form

$$A_{far}, B_{far} = a_{A,B} \mp |b_{A,B} \sin(c_{A,B}\theta)| \mp |d_{A,B} \cos(2c_{A,B}\theta)| \mp e_{A,B} \cos(4c_{A,B}\theta) \quad (3.5)$$

where the subtraction sign is chosen for parameter A_{far} , and addition for parameter B_{far} . Once again the period parameter $c_A = c_B$, with the result being that 9 separate parameters must be determined to generate the fit to the region $1.5 < r < 2.0$ cm. The fit does not extend further because the azimuthal dependence of the parameters at radii greater than 2 cm becomes too convoluted to reliably fit to with any nice function and/or a feasible number of parameters, and so the two-dimensional model in its current form effectively excludes the corners and near edges of the cell.

Thus we find ourselves with two separate drift-time relations, with a total of 14 parameters all dependent upon cell geometry, gas composition and anode voltage. Whilst the geometry is unlikely to change, the gas composition may change during trial runs and the voltages of each cell are likely to be tweaked on a cell-by-cell basis to account for minor differences in construction and cell ageing. The disadvantage of the two-dimensional fit model becomes clear: whenever any change is made to the cell, the fit has to be painstakingly redone to extract the new parameters.

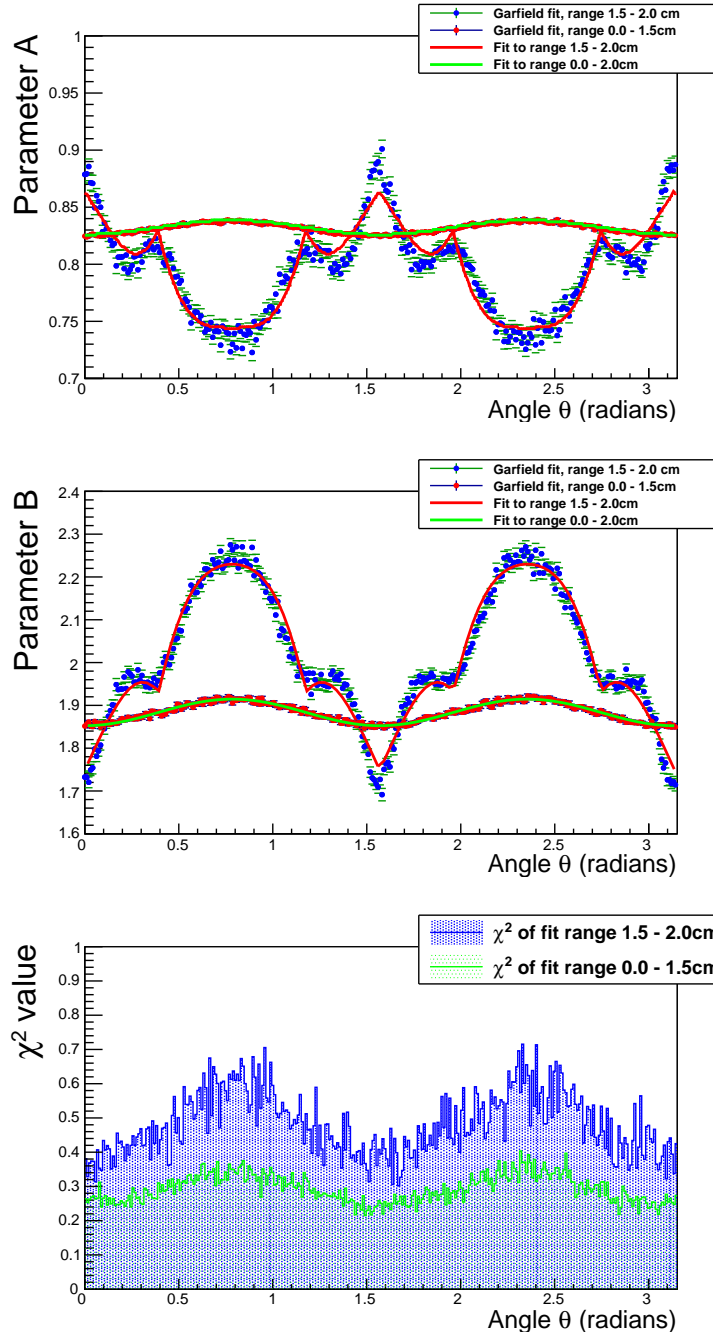


Figure 3.3: Plotting parameters A and B of Equation 3.3 against azimuthal angle θ . Both parameters have been fitted with equation FITEQUATION

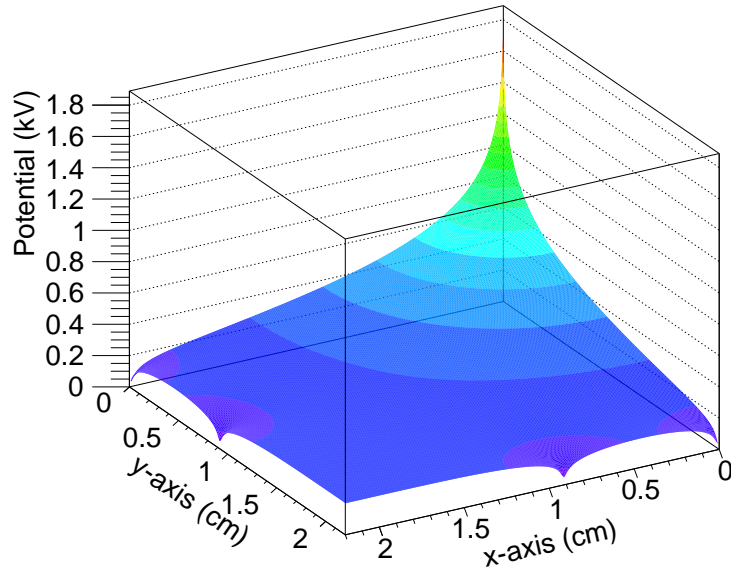


Figure 3.4: The potential field in a standard SuperNEMO quarter cell, as determined by the CellSolver program.

3.2.2 The timemap model

An alternative to the 2D fit introduced in the previous section is to generate a timemap – a one-to-one distribution of (x, y) to t_{drift} – that can be interpolated during digitization. The timemap program is in essence a mini-GARFIELD implemented into the structure of the digitization process, capable of solving for the potential field in a cell and simulating the drift of electrons from each point on an evenly spaced grid to the anode wire. The drift time for a given POCI can then be interpolated from the timemap.

The potential field for a cell cross-section is solved via a successive over-relaxation (SOR) method, using a version of the CellSolver program incorporated into the timemap code. Due to the symmetry of the problem, only a quarter-cell cross-section is considered, with the wires being given as point-like Dirichlet conditions of finite voltage in the solution to Poisson’s equation; the remaining boundaries are considered as Neumann conditions. The resulting potential field map for a cell operating at 1.81 kV is shown in Figure 3.4.

The potential field map solver has been tested using both the standard check $\epsilon_0 \nabla^2 \phi = \rho$

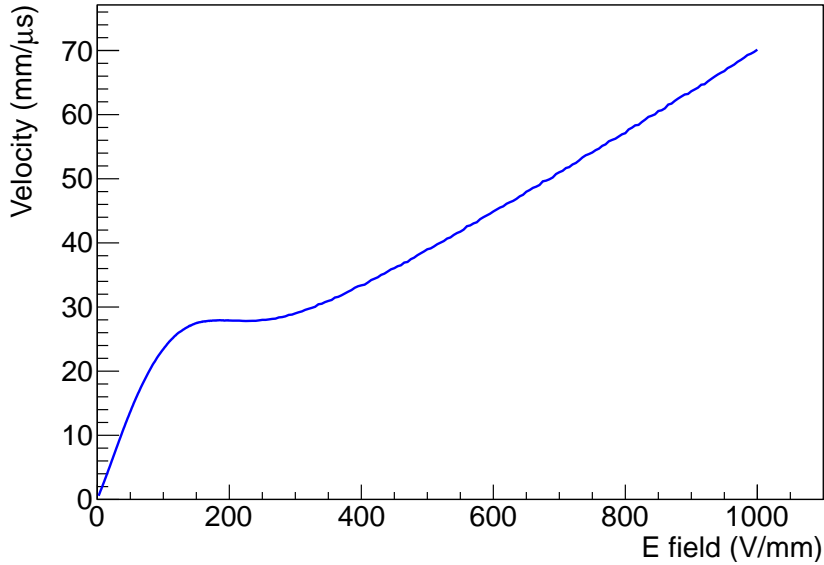


Figure 3.5: The drift velocity to electric field relation, as calculated using MAGBOLTZ with the SuperNEMO gas mixture.

and by comparison to a field map generated by the commercial software FlexPDE - in both cases, the solver demonstrates more than sufficient precision for our purposes. Following this, the gradient is taken to obtain the electric field map for the cell. The program MAGBOLTZ is used to build a relation between electron drift velocity and electric field; this is shown in Figure 3.5.

With the electric field map in place and the velocity-field relation known, the electron drift is simulated at each point on the grid to generate the time map. This is done by an improved Euler two-step method, where

$$\mathbf{r}'_{n+1} = \mathbf{r}_n + \frac{1}{2}(\mathbf{v}_n + \mathbf{v}_{n+1}) dt \quad (3.6)$$

with \mathbf{v}_n being the velocity at step n corresponding to an electric field \mathbf{E} at the point \mathbf{r}_n . Practically, each step is made in two parts; first, the velocity at the point \mathbf{r}_n is calculated and the step performed according to the simpler Euler step-wise method, i.e.

that $\mathbf{r}_{n+1} = \mathbf{r}_n + \mathbf{v}_n dt$. The velocity \mathbf{v}_{n+1} is calculated at the new location and the step is then undone, being redone using the average being \mathbf{v}_n and \mathbf{v}_{n+1} ; hence the new location \mathbf{r}'_{n+1} is not the “true” position corresponding to the velocity \mathbf{v}_{n+1} but rather an improved step calculation given by the foreknowledge of the latter. Being a second-order method, the error in each step is on the order of dt^3 , and to avoid excessively large steps in regions of high field (such as in the proximity of the wire) the step size $d\mathbf{r}$ is constrained to a value of half the wire thickness, and the step time $dt = \frac{dr}{v_n}$. Furthermore, the step time itself is constrained such that if $\frac{dr}{v_n} > dt_{limit}$, the method forces $dt = dt_{limit}$, where dt_{limit} is a user-defined limit on the time step.

Equation 3.6 does not explicitly account for diffusion, which is important in regions of low electric field when the rms displacement due to diffusion is on the order of the drift velocity. To implement this into the drift we consider the movement associated with the two separate diffusion coefficients D_L and D_T introduced in section 2.2.2. As discussed previously, the spread of an electron cluster along an axis is described by a gaussian with a standard deviation as given in Equation 2.16; thus to calculate the effect of diffusion, we consider the movement of the edge of the cluster that is closest to the wire. With every step of Equation 3.6 we consider the diffusion from the point on this edge in the direction of the wire. Given this, the drift due to diffusion in the direction of the wire after a time step dt is

$$d\mathbf{r}^{(D)} = \left(2 \cos \theta \sqrt{2D_L dt} + 2 \sin \theta \sqrt{2D_T dt} \right) \hat{\mathbf{r}}_n \quad (3.7)$$

where $\hat{\mathbf{r}}_n$ is the unit vector in the direction of the position vector relative to the wire \mathbf{r}_n and θ is the angle between $\hat{\mathbf{r}}_n$ and the vector in the direction of the electric field at the point \mathbf{r}_n . When the electric field falls below a user-specified threshold, the step is made using a modified version of Equation 3.6, given as

$$\mathbf{r}'_{n+1} = \mathbf{r}_n + \frac{1}{2}(\mathbf{v}_n + \mathbf{v}_{n+1}) dt - \frac{1}{2} \left(d\mathbf{r}_n^{(D)} + d\mathbf{r}_{n+1}^{(D)} \right). \quad (3.8)$$

The choice of the electric field below which the diffusion Equation 3.8 is used is determined primarily by the ratio $d\mathbf{r}_n^{(D)}/\mathbf{v}(\mathbf{E})_n dt$ and by the value of the electron anisotropy; both can be determined using the MAGBOLTZ program. Alternatively, the simulation can be run with the diffusion Equation 3.8 being used at all electric fields.

An alternative approach to including diffusion is to use Equation 3.6 whenever the drift due to the electric field in the direction of the wire is greater than the drift due to the diffusion, i.e. $\mathbf{v}_n \cdot (-\hat{\mathbf{r}}) > d\mathbf{r}_n^{(D)}$. When this is not the case we make a step using only the drift due to diffusion, such that

$$\mathbf{r}'_{n+1} = \begin{cases} \mathbf{r}_n - \frac{1}{2} \left(d\mathbf{r}_n^{(D)} + d\mathbf{r}_{n+1}^{(D)} \right) & \text{if } -\hat{\mathbf{r}} \cdot \mathbf{v}_n dt < d\mathbf{r}_n^{(D)} \text{ and} \\ \mathbf{r}_n + \frac{1}{2}(\mathbf{v}_n + \mathbf{v}_{n+1}) & \text{otherwise.} \end{cases} \quad (3.9)$$

To summarise, we have four options available to us when using the timemap model: no diffusion (exclusively Equation 3.6), diffusion below a user-defined electric field (Equations 3.6 and 3.8), diffusion at all fields (exclusively Equation 3.8) and diffusion being considered separately from the electric field drift (Equation 3.9). Of these four, the one most in agreement with an equivalent timemap generated using GARFIELD is the method using Equation 3.9. The timemap generated using Equation 3.9 is shown in Figure 3.6 (a) and the equivalent timemap generated using GARFIELD is shown in Figure 3.6 (b). Figure 3.6 (c) shows the absolute difference between the GARFIELD value and the timemap model, given as a percentage of the GARFIELD value; it is reassuring to see that for most of the quarter cell, the two agree to within 10%. A timemap generated using the two-dimensional fit model is shown in Figure 3.6 (d).

In the presence of a magnetic field, we rely on Tonk's theorem as discussed in section 2.2.2 to model the electron drift without having to regenerate the MAGBOLTZ input. We

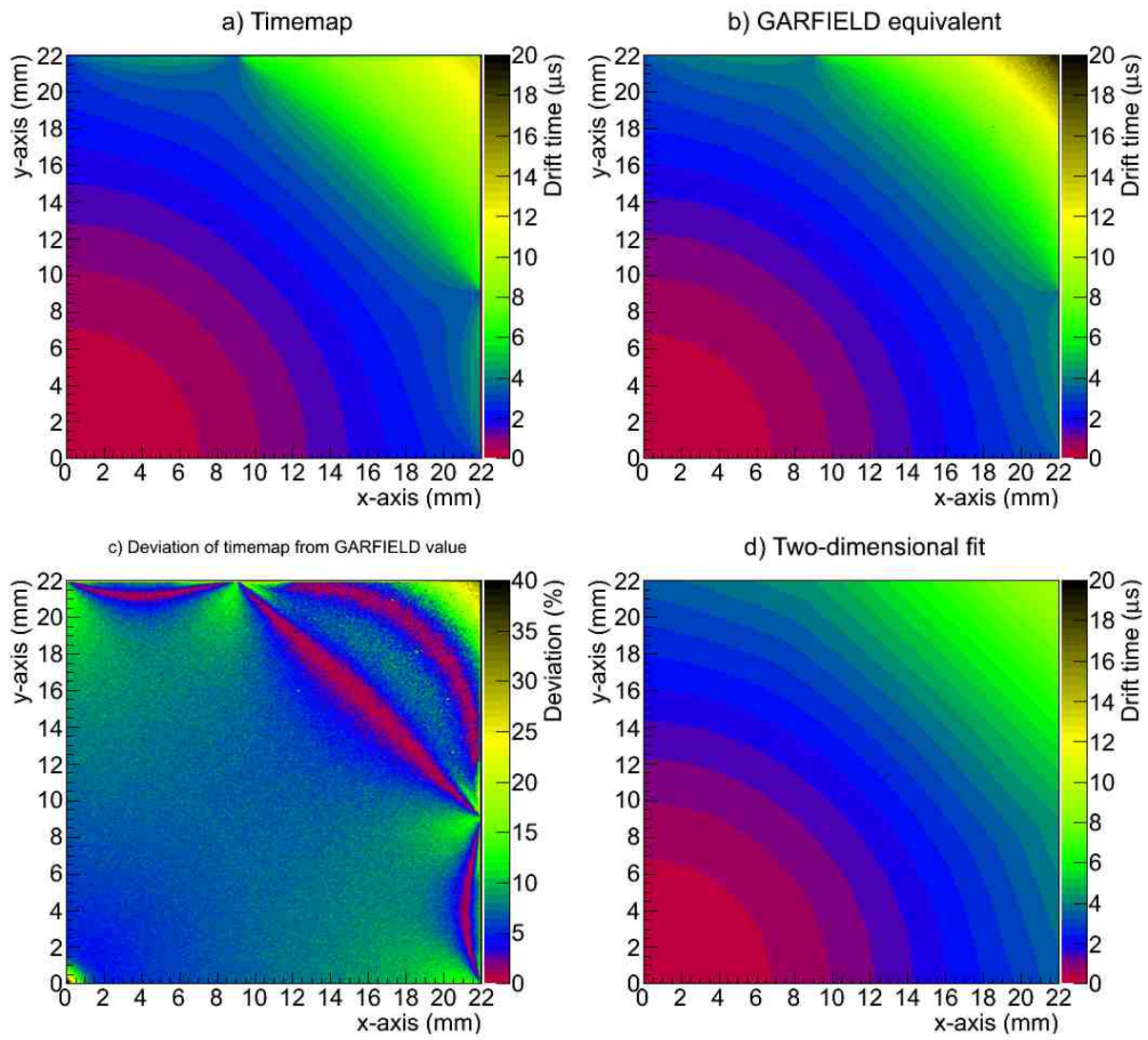


Figure 3.6: CAPTION HERE

assume that over a step $d\mathbf{r}$ the mean time τ between collisions is constant, and that the electric field is orthogonal to the magnetic field. The direction of the drift velocity is given by equation 2.14 and its magnitude by

$$|\mathbf{u}| = |\mathbf{u}_B| \cos(\phi) , \quad (3.10)$$

where \mathbf{u}_B is the magnitude of the drift velocity in the absence of a magnetic field. The step is then made using this modified drift vector.

In terms of computational efficiency, the timemap in figure TIMEMAPCOMPARISON took 16 minutes 45 seconds to generate on one core of a 64-bit Intel Core 2 Duo at 1.86 GHz, compared to the GARFIELD timemap which took 17 minutes 50 seconds on a 32-bit Intel Pentium M at 1.86 GHz. The efficiency of the timemap model can be further enhanced by enabling the dual-step method, in which a longer step size is used for steps greater than a user-defined radius from the wire, shrinking to a small step size once the step enters this radius. It is also possible to load a CellSolver field solution generated earlier, reducing the previous calculation to 15 minutes 28 seconds. Once generated, extracting a value from the timemap is an $O(1)$ operation; it is simply an interpolated lookup table.

We can thus conclude that the timemap model, particularly that which uses Equation 3.9, is the most effective in replicating the drift times given by GARFIELD. Aside from at the corners of the cell, the two agree to within 10% and are of comparable computational efficiency. The timemap model is more effective than the two-dimensional fit model since it does not require that the input data from third-party programs be regenerated when the voltage or geometry changes, and can also account for the presence of a magnetic field.

3.3 Resolution of the simulated drift time

Both the two-dimensional fit and the timemap model are one-to-one relations – two separate events in the simulation with the same POCI will give the same drift time. To account for

the resolution in the drift times that arises due to random fluctuations, the interpolated time given by the models must be smeared using a gaussian probability distribution with some position-dependent standard deviation.

Equation 2.20 furnishes us with such a value, but at second glance may prove to be an incorrect choice. The length of the track through the cell is, in the case of the simulation, inversely proportional to the resolution of the cell; a glancing track passing through the corner of the cell and the comparatively long drift distance provides more scope for random fluctuations than the longer track associated with a path passing very close to the anode wire. A GARFIELD Monte Carlo simulation showed that for a given radius r from the anode, the distribution of drift times associated with the ring r to $r+dr$ is well described by a gaussian of mean t_{drift} and standard deviation σ_t , with the standard deviation increasing with r . At radii beyond $r = 1.4$ cm the electric field loses azimuthal symmetry, and the gaussian distribution changes into a superposition of Gaussians, each one associated with an angular area $\theta + d\theta$. Although a two-dimensional extrapolation of the resolution is a possibility, in the same manner as was done for the drift time in section 3.2.1, for the sake of simplicity we use a one-dimensional relation fitted to those Gaussians for which $r < 1.4$ cm. The values of σ_t taken from the GARFIELD data and the subsequent fit to these are shown in Figure 3.7.

The result is that for a helium/neon/alcohol mixture in the ratio 94/2/4 percent, the resolution associated with a drift time t_{drift} given by either of the models is

$$\sigma_t = 0.0017 + 0.0166 t_{drift} \tag{3.11}$$

where σ_t and t_{drift} are given in μs .

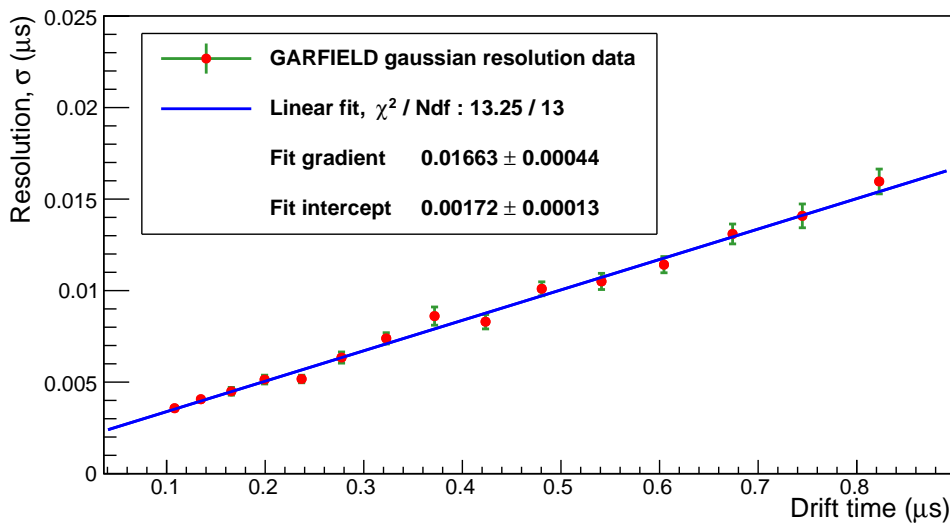


Figure 3.7: Plot of the standard deviations of the gaussians used to fit the distribution of drift times at a given radius, using the GARFIELD Monte Carlo.

3.4 Implementation in the digitization process

As mentioned earlier in section 2.4.1, the SNWARE software is developed such that custom user modules can be implemented during or immediately after the simulation. When running the SNWARE software without any modules, the output is a file containing each event stored sequentially as a serialized C++ container class; this format is referred to as *simulated data*. A digitization module would be loaded into the software chain at run-time to convert the simulated data into the digitized data, which in the nomenclature of the collaboration is referred to as *calibrated data*. If desired, the Timemap package would be incorporated into such a module for use at runtime.

To avoid having to run the simulation each time, both the timemap class and the two-dimensional fit model have been developed as C++ classes for use either in an SNWARE module or a stand-alone program; in this study, they are used in the latter incarnation. The simulated data is loaded into the stand-alone program and the two models are applied to the POCI extracted from each event, and stored as calibrated data. Although the

Timemap class can be used in a program external to Falaise, it is not independent of SNWARE entirely since it relies upon the datatools module present in Bayeux for the purposes of configuration and data input/output.

Chapter 4

Comparison of the models to experimental data

In this chapter we compare the results of a simulation done using both the two-dimensional fit model and timemap interpolation against data taken using a SuperNEMO 18-cell module in use at the University of Manchester. The SNWARE simulation has been adapted to reflect the geometry and physics of the 18-cell module, which is coupled to a photomultiplier tube (PMT) that serves as the event trigger.

4.1 The SuperNEMO cell in Manchester

The 18-cell module is 9 cells wide by 2 cells deep and kept in a sealed tank that contains the gas mixture. Placed directly on top of the tank, vertically in line with the central cell, is a scintillator with an attached PMT. The anodes of each cell are connected directly to the analogue-to-digital converter (ADC). Unlike previous prototype cells, the derivative signal is not taken; instead, this is calculated later during analysis. The cathode signals are not used during this experiment and hence are not connected to the ADC. A simplified schematic of the setup is shown in Figure 4.1.

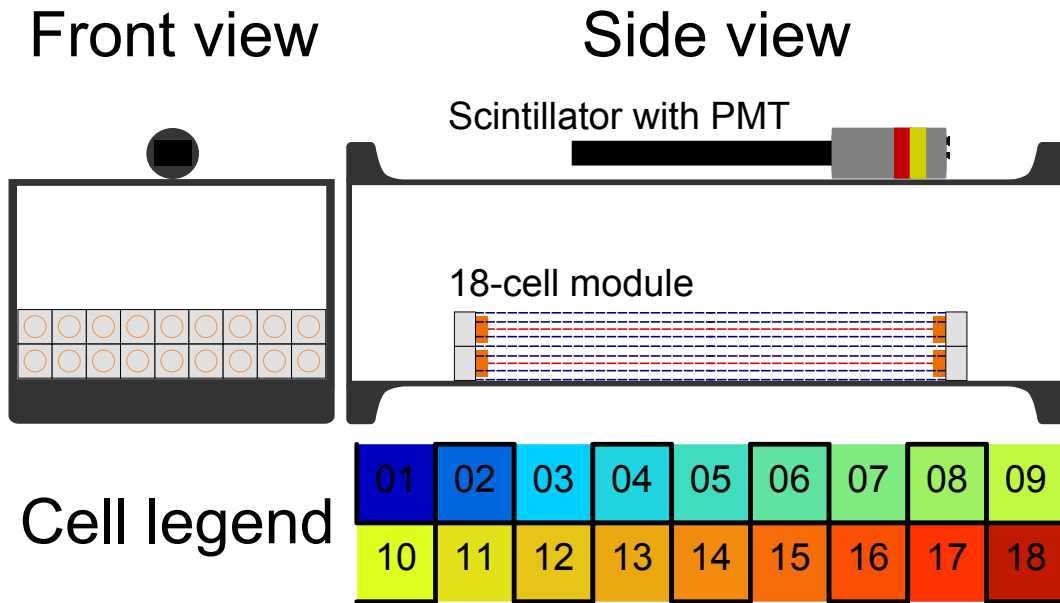


Figure 4.1: A simplified diagram of the experimental setup in the cleanroom. The relative locations of the PMT on top of the tank and the cell inside the tank are given. The cell is contained within a bar frame that gives it rigidity.

The acquisition triggered on the passage of a particle through the PMT and any one of cells 01 to 07. The PMT signal is passed through a gate unit before connecting to the ADC; any signal from one of the aforementioned cells within a $35 \mu\text{s}$ window following the PMT signal is registered as a coincidence and saves the event to file.

An uninterrupted data run of 29,400 events was taken over the course of 20 hours, with each cell operating at 1.7 kV and the PMT at 1.8 kV. The gas mixture the cell was helium/neon/argon in the ratio 94/2/4 percent, at room temperature and pressure.

The collected data is passed through an analysis program that applies the following cuts to the dataset:

1. Cell 13 must have fired.
2. The value $t_{anode} > t_{pmt}$.
3. The pedestal value must be greater than 760 mV and less than 800 mV.

4. Either cell 03, 04 or 05 must have fired.
5. No other cells must have fired.
6. The value of t_{pmt} must be greater than $48 \mu s$ and less than $52 \mu s$.
7. If cell 03 fired, cell 05 must not have fired, and viceversa.

The requirement that $48 < t_{pmt} < 52 \mu s$ is because the trigger signal, by the settings on the ADC, should lie at $50 \mu s$ in the trigger window.

Out of 28,400 events, 3207 survive the cuts. From these events, we take the drift time to be $t_{drift} = t_{anode} - t_{pmt}$ and plot the drift time distribution. To remove background events due to random coincidences, we make a linear fit to the region 30 to $59 \mu s$ (in which we do not expect there to be any legitimate signals) and remove from each bin the value of the offset given by the fit. The drift time distribution extracted from the data (both with and without background removed) is shown in Figure ??.

4.2 Applying the models

To simulate the cleanroom setup, a special SNWARE run was made with a modified geometry to mimic that in Figure 4.1. A single supernemo cell located within a tank, placed directly beneath a block serving as the scintillator trigger. Cosmic muons, in a ratio μ^+/μ^- of 1.2, are generated directly above the scintillator block, with an energy distribution described by a gaussian of mean 4 GeV and standard deviation 1 GeV. Each particle was generated pointing downwards toward the cell, with a momentum lying within a cone of 70° . The zenith of the particle's direction was governed by a probability distribution function of shape $\cos^2 \theta$. If the particle entered the drift cell, ionisation clusters were generated along its track in the manner described in section 2.2.1 and the POCI were saved to disk.

This simulation data file was then converted into calibrated data, in the manner described in section 3.4, using both the timemap and two-dimensional fit models. For the

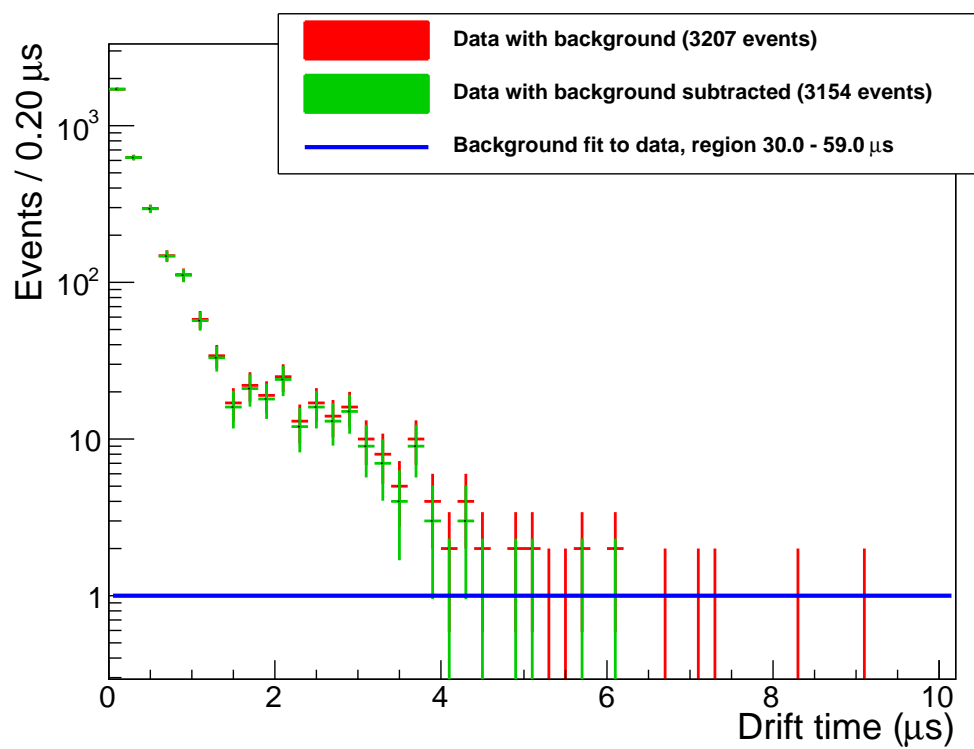


Figure 4.2: CAPTION HERE

timemap model, the effects of diffusion were considered in three separate stages; no diffusion, diffusion only at fields less than 1 V/mm, and diffusion at all fields. The resulting 4 sets of calibrated data are shown plotted against the data set from section 4.1 in Figure 4.3. Each data set was normalized to represent a distribution due to 10,000 events.

It is immediately evident that, although the timemap and two-dimensional fit model agree to a good extent, neither one of these matches the excess of short drift times seen in the data. Since the timemap model produces similar results to those of the two-dimensional fit (and, by extension, GARFIELD), it is possible that the distribution of POCI within the simulation has been miscalculated.

It is immediately evident from Figure 4.3 that, although the timemap and two-dimensional fit model agree to a good extent, neither one of these matches the excess of short drift time seen in the data. When considering the individual components of the simulation, the timemap model has already been shown to agree with GARFIELD to within 10%. Furthermore, the model used to generate cosmic ray muons in the simulation, although simplified, is unlikely to be inaccurate enough to account for the discrepancy. The cuts made in section 4.1 ensure that the data in Figure 4.3 results only from events where a single particle descended through the PMT triggered the cell, so the simulation geometry and particle generation should be an accurate representation of the physics. This leads us to conclude that the most likely outcome is that the discrepancy is due to an inaccuracy in how the ionisation process is simulated and the resulting POCI are generated. In the next section we will investigate to what degree a re-distribution of the POCI can affect the outcome of the simulation.

4.3 Re-distributing the POCI

The distribution of POCI generated with the SNWARE simulation, which uses the ionisation process described in section 2.2.1, is shown in Figure 4.4 (a). In an attempt to

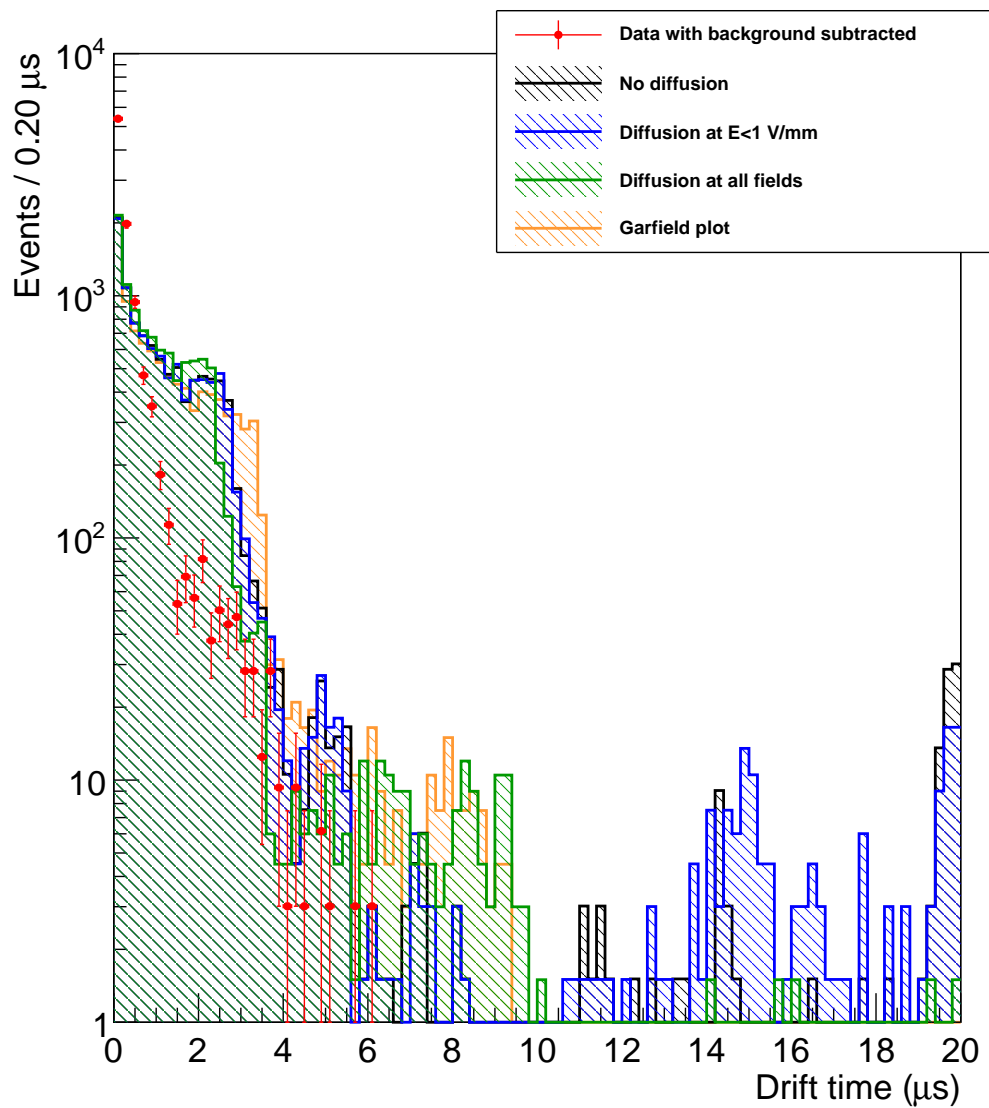


Figure 4.3: The timemap model and GARFIELD two-dimensional fit against the data from the 18 cells data run. The distributions have been normalized to represent a total of 10,000 events

reconcile the simulation with the data, we generate a new distribution using a random number generator [43] and separate probability density functions for the x and y axes.

We generate each POCI by separately sampling its x and y coordinate from a probability density function (PDF). The PDF for the y -coordinate is given by a gaussian with a standard deviation of 0.1 cm, whilst the PDF for the x -coordinate is a gaussian with a standard deviation of 0.58 cm and a linear offset. The generator does not allow POCI to be generated inside or within 40 microns of the wire. This combination of PDFs was chosen because it supposes that the ionisation process described in section 2.2.1 is largely correct but that those POCI at radii greater than 1 cm are much less effective than those closer to the wire due to some unknown factor. The distribution of 10,000 POCI generated using these PDFs is shown in Figure 4.4 (b).

The result of applying the timemap and two-dimensional fit models to the distribution of POCI in Figure 4.4 (b) in the same manner as in section 4.2 and Figure 4.3 is shown in Figure 4.5. With the re-distributed POCI the simulation is a far better match to the data than was seen in Figure 4.3; this appears to confirm that the discrepancy is due to an inaccuracy in the ionisation process that the simulation uses to generate the POCI. Whether this hypothesis is correct, and what modifications will have to be made to the ionisation process if it is are the scope for future work.

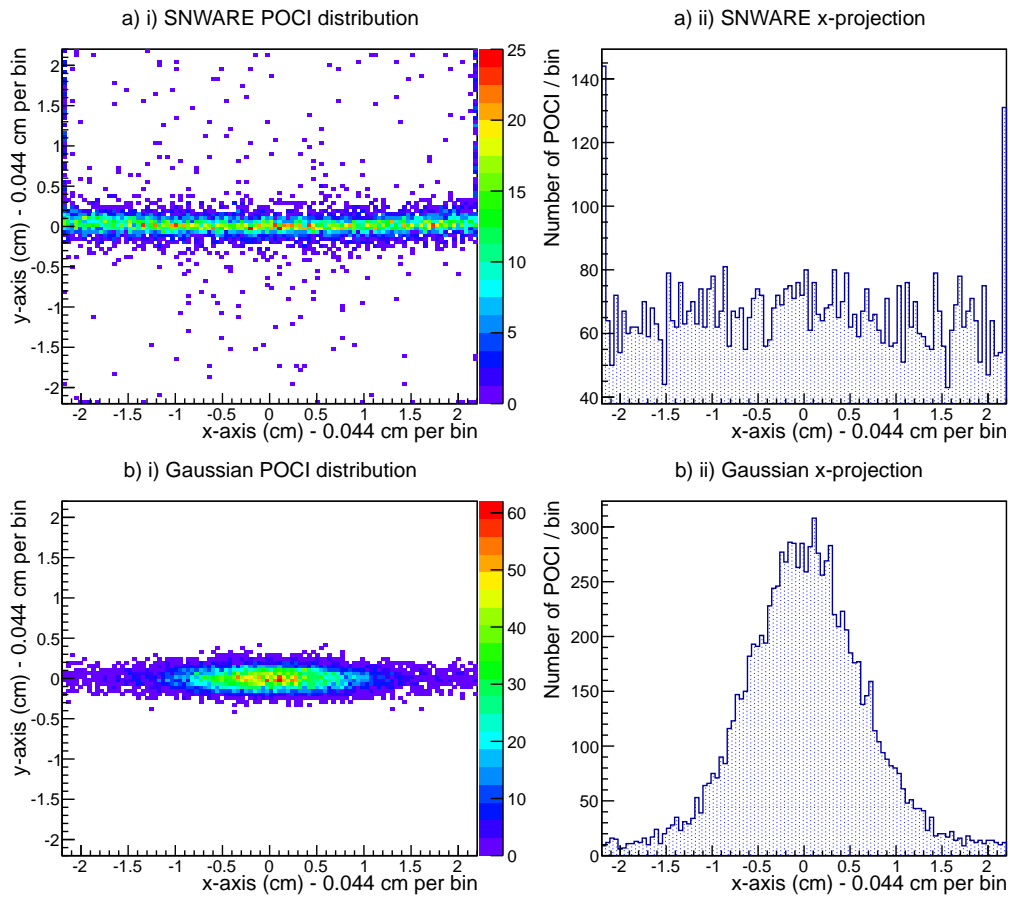


Figure 4.4: The distribution of POCI in the cell, as given by the SNWARE simulation discussed in section 4.2

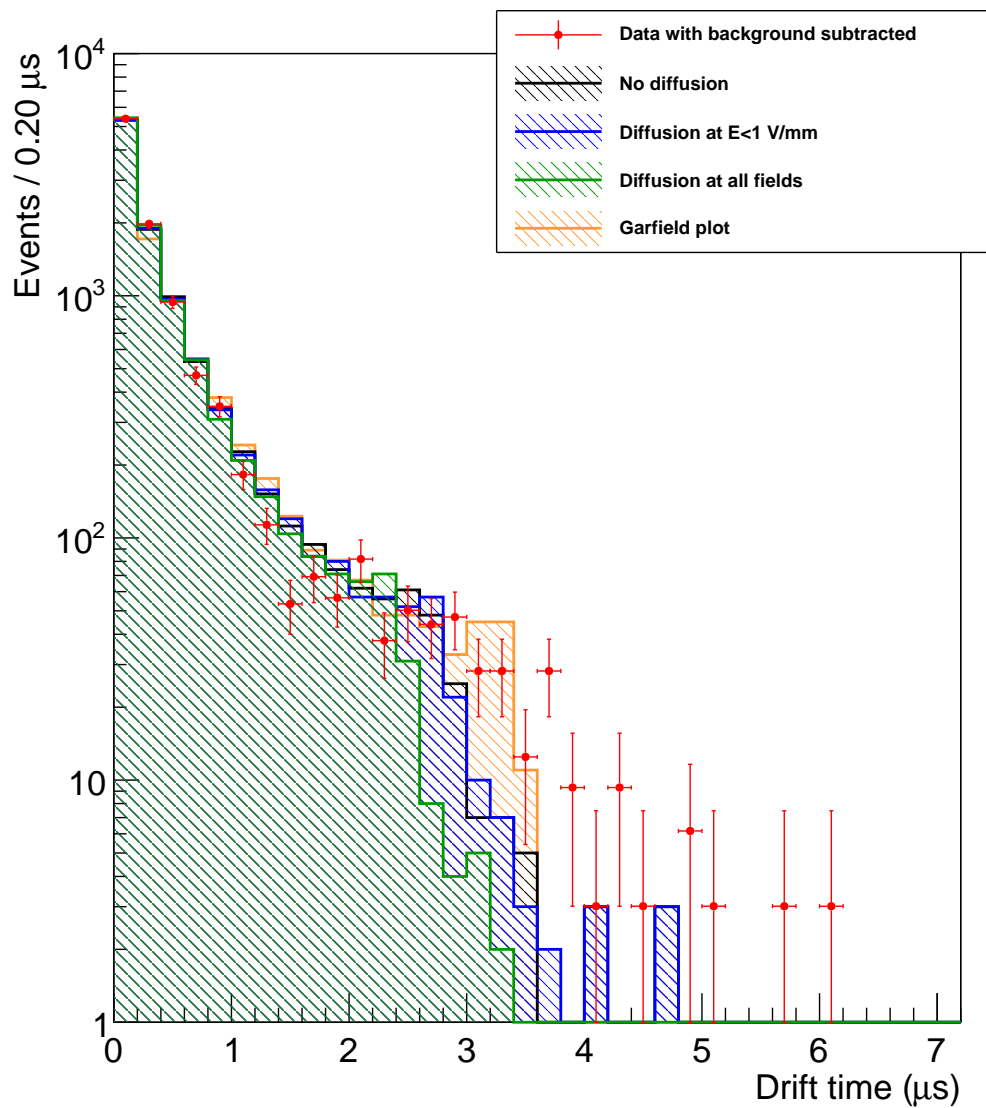


Figure 4.5: The timemap model and GARFIELD two-dimensional fit, generated using the distribution of POCI in Figure 4.4, against the data from the 18 cells. The histograms have been normalized to represent a total of 10,000 events.

Chapter 5

Conclusion

5.1 The cathode simulation

Although only lightly touched upon, studies of the propagation time discussed in section 3.1 indicate that the simulation method used in NEMO3 is more than adequate for the purposes of SuperNEMO. The only change that need be made is to account for the reduction in plasma propagation velocity at short event delays. However, since the reconstruction method described in section 2.3 relies upon the ratio of the cathode times and not their actual value, this is of little consequence; what remains important however is that the efficiency of the plasma propagation be well known. Unfortunately, this study has little to offer in that regard.

5.2 Feasibility of the two models

With the re-distributed POCI of Figure 4.4, both the timemap model and two-dimensional fit model are in good agreement with the data; more importantly, however, they are in good agreement with each other. In fact, the timemap model is in very good agreement with GARFIELD itself for radii less than 2.2 cm, and it is only in the corners of the cell that

the timemap appears to overestimate the drift time. This is due to the low electric field in that region, and the addition of diffusion at low electric fields reconciles the timemap with GARFIELD.

As such, the timemap model demonstrates itself to be a feasible alternative to the two-dimensional model or the explicit use of GARFIELD in the digitization process. Although the initial generation of the timemap is more time-consuming than using GARFIELD, once the timemap is generated the interpolation process is faster than the GARFIELD Monte Carlo drift function. Furthermore, the timemap is simpler and offers greater ease of use than GARFIELD, as well as the principal advantage being that it can be incorporated into the C++ code of an SWARE module.

5.3 Final remarks

References

- [1] D. Griffiths, *Introduction to Elementary Particles*. Wiley-VCH, 2009.
- [2] C. L. Cowan, Jr., F. Reines, F. B. Harrison, H. W. Kruse, and A. D. McGuire, “Detection of the Free Neutrino: A Confirmation,” *Science*, vol. 124, pp. 103–104, July 1956.
- [3] Wikimedia, “Standard model of elementary particles.” Licensed under Creative Commons 3.0.
- [4] K. Nakamura *et al.*, “Review of particle physics,” *J.Phys.G*, vol. G37, p. 075021, 2010.
- [5] Y. Fukuda *et al.*, “Evidence for oscillation of atmospheric neutrinos,” *Phys. Rev. Lett.*, vol. 81, pp. 1562–1567, Aug 1998.
- [6] Q. Ahmad *et al.*, “Measurement of the rate of $\nu/e + d \rightarrow p + p + e^-$ interactions produced by B-8 solar neutrinos at the Sudbury Neutrino Observatory,” *Phys.Rev.Lett.*, vol. 87, p. 071301, 2001.
- [7] K. Eguchi *et al.*, “First results from KamLAND: Evidence for reactor anti-neutrino disappearance,” *Phys.Rev.Lett.*, vol. 90, p. 021802, 2003.
- [8] M. Goeppert-Mayer, “Double beta-disintegration,” *Phys. Rev.*, vol. 48, pp. 512–516, Sep 1935.

- [9] M. G. Inghram and J. H. Reynolds, “Double beta-decay of ^{130}Te ,” *Phys. Rev.*, vol. 78, pp. 822–823, June 1950.
- [10] A. Barabash, “Average (recommended) half life values for two neutrino double beta decay,” *Czech.J.Phys.*, vol. 52, pp. 567–573, 2002.
- [11] S. King, *Measurement of the Double Beta Decay Half-Life of ^{100}Mo to the 0_1^+ Excited State, and ^{48}Ca to the Ground State in the NEMO 3 Experiment*. PhD thesis, University College London, October 2008.
- [12] A. Barabash, “Average and recommended half-life values for two neutrino double beta decay: Upgrade-09,” *AIP Conf.Proc.*, vol. 1180, pp. 6–15, 2009.
- [13] R. Arnold et al., “Measurement of the $\beta\beta$ decay half-life of ^{130}Te with the nemo-3 detector,” *Phys. Rev. Lett.*, vol. 107, p. 062504, Aug 2011.
- [14] N. Ackerman et al., “Observation of two-neutrino double-beta decay in ^{136}Xe with the exo-200 detector,” *Phys. Rev. Lett.*, vol. 107, p. 212501, Nov 2011.
- [15] W. Furry, “On transition probabilities in double beta-disintegration,” *Phys.Rev.*, vol. 56, pp. 1184–1193, 1939.
- [16] F. Avignone, R. Brodzinski, *et al.*, “The international germanium experiment (IGEX) in 1993,” *Nuclear Physics B - Proceedings Supplements*, vol. 35, no. 0, pp. 354 – 357, 1994.
- [17] H. Klapdor-Kleingrothaus, “The HEIDELBERG-MOSCOW Ge-76 double beta experiment in Gran Sasso 1990-2003 and status of absolute neutrino mass,” pp. 307–364, 2003.
- [18] E. Previtali, C. Arnaboldi, D. Artusa, F. Avignone, M. Balata, *et al.*, “CUORICINO: A new large bolometer array for astroparticle physics,” *Nucl.Instrum.Meth.*, vol. A518, pp. 256–258, 2004.

- [19] H. Simgen, “Gerda: A new 76Ge double beta decay experiment at gran sasso,” *Nuclear Physics B - Proceedings Supplements*, vol. 143, no. 0, p. 567, 2005.
- [20] L. Ejzak, “The Search for Neutrinoless Double Beta Decay in CUORE,” 2009.
- [21] K. Kume, K. Fushimi, R. Hazama, M. Kawasaki, N. Kudomi, *et al.*, “Double beta decays studied by ELEGANT,” pp. 490–495, 1995.
- [22] R. Arnold, C. Augier, *et al.*, “Technical design and performance of the nemo 3 detector,” *Nuclear Instruments and Methods in Physics Research Section A: Accelerators, Spectrometers, Detectors and Associated Equipment*, vol. 536, pp. 79 – 122, 2005.
- [23] R. Arnold *et al.*, “Measurement of double beta decay of Mo-100 to excited states in the NEMO 3 experiment,” *Nucl.Phys.*, vol. A781, pp. 209–226, 2007.
- [24] J. Argyriades *et al.*, “Measurement of the Double Beta Decay Half-life of Nd-150 and Search for Neutrinoless Decay Modes with the NEMO-3 Detector,” *Phys.Rev.*, vol. C80, p. 032501, 2009.
- [25] H. Klapdor-Kleingrothaus, A. Dietz, L. Baudis, G. Heusser, I. Krivosheina, *et al.*, “Latest results from the Heidelberg-Moscow double beta decay experiment,” *Eur.Phys.J.*, vol. A12, pp. 147–154, 2001.
- [26] H. Klapdor-Kleingrothaus, “Status of evidence for neutrinoless double beta decay, and the future: GENIUS and GENIUS TF,” pp. 263–282, 2003.
- [27] C. Aalseth, I. Avignone, F.T., A. Barabash, F. Boehm, R. Brodzinski, *et al.*, “Comment on ‘Evidence for neutrinoless double beta decay’,” *Mod.Phys.Lett.*, vol. A17, pp. 1475–1478, 2002.

- [28] R. Arnold *et al.*, “Probing New Physics Models of Neutrinoless Double Beta Decay with SuperNEMO,” *Eur.Phys.J.*, vol. C70, pp. 927–943, 2010.
- [29] F. Mauger. Internal communication.
- [30] W. Blum and L. Rolandi, *Particle Detection with Drift Chambers*. Springer-Verlag, 1994.
- [31] A. Peisert and F. Sauli, *Drift and diffusion of electrons in gases: a compilation (with an introduction to the use of computing programs)*. Geneva: CERN, 1984.
- [32] L. Tonks, “Particle transport, electric currents, and pressure balance in a magnetically immobilized plasma,” *Phys. Rev.*, vol. 97, pp. 1443–1445, Mar 1955.
- [33] E. B. Wagner, F. J. Davis, and G. S. Hurst, “Time-of-Flight Investigations of Electron Transport in Some Atomic and Molecular Gases,” *J. Chem. Phys.*, vol. 47, pp. 3138–3147, Nov. 1967.
- [34] K. F. Ness, “Spherical-harmonics decomposition of the boltzmann equation for charged-particle swarms in the presence of both electric and magnetic fields,” *Phys. Rev. E*, vol. 47, pp. 327–342, Jan 1993.
- [35] G. W. Fraser and E. Mathieson, “Monte Carlo calculation of electron transport coefficients in counting gas mixtures I. Argon-methane mixtures,” *Nuclear Instruments and Methods in Physics Research A*, vol. 247, pp. 544–565, July 1986.
- [36] C. Augier, R. Arnold, J. Baker, A. Barabash, G. Broudin, V. Brudanin, A. Cafrey, V. Egorov, A., K. Errahmane, A. Etienvre, J. Guyonnet, F. Hubert, P. Hubert, C. Jollet, S. Jullian, O. Kochetov, V. Kovalenko, V., S. Konovalov, D. Lalanne, K. Lang, F. Leccia, C. Longuemare, G. Lutter, C. Marquet, F. Mauger, H. Ohsumi, F. Piquemal, J. Reyss, R. Saakyan, X. Sarazin, L. Simard, Y. Shitov, A. Smolnikov, I. Stekl, C. Sutton, G. Szklarz, J. Thomas, V. Timkin, V. Tretyak, V. Umatov, L. Vala,

- I. Vanushin, V. Vasilyev, V. Vorobel, and T. Vylov, “Technical performance of the NEMO 3 detector ”Advantages and limitations”,” tech. rep., 2005. Corinne AUGIER for the NEMO Collaboration.
- [37] F. Mauger, M. Bongrand, X. Garrido, B. Guillon, Y. Shitov, and F. Nova, *SNWARE software chain*. version 2.0 β , 2012.
- [38] S. Biagi, *MAGBOLTZ*. version 9.0.1, May 2012.
- [39] R. Veenhof, *GARFIELD*. version 9, September 2010.
- [40] D. Teresi, *CellSolver*. version 1.0, November 2011.
- [41] I. Smirnov, *HEED*. version 1.01, March 1997.
- [42] E. Chaveau. Internal communication.
- [43] M. Matsumoto and T. Nishimura, “Mersenne Twistor: A 623-dimensionally equidistributed uniform pseudorandom number generator,” *ACM Transactions on Modeling and Computer simulation*, vol. 8, pp. 3–30, January 1998.